ADVANCED MATERIALS
www.advmat.de

Chiral Perovskites for Next-Generation Photonics: From Chirality Transfer to Chiroptical Activity

*Sunihl Ma, Jihoon Ahn, and Jooho Moon**

Organic–inorganic hybrid halide perovskites (OIHPs) are commonly used as prototypical materials for various applications, including photovoltaics, photodetectors, and light-emitting devices. Since the chiroptical properties of OIHPs are deciphered in 2017, chiral OIHPs have been rediscovered as new hybrid systems comprising chiral organic molecules and achiral inorganic octahedral layers. Owing to their exceptional optoelectrical properties and structural flexibility, chiral OIHPs have received a considerable amount of attention in chiral photonics, chiroptoelectronics, spintronics, and ferroelectrics. Despite their intriguing chiral properties, the transfer mechanism from chiral molecules to achiral semiconductors has not been extensively investigated. Furthermore, an in-depth understanding of the origin of chiroptical activity is still elusive. In this review article, recent advances in the chiroptical activities of chiral OIHPs and polarization-based devices adopting chiral OIHPs are comprehensively discussed, and insight into the underlying chirality transfer mechanism based on theoretical considerations is provided. This comprehensive survey, with an emphasis on the chirality transfer mechanism, will help readers understand the chiroptical properties of OIHPs, which are crucial for the development of spin-based photonic and optoelectronic devices. Additionally, promising strategies to exploit the potential of chiral OIHPs are also discussed.

1. Introduction

Chiral photonics based on chiral materials is a highly active research topic that is associated with various applications, such as quantum communication,[1] optical spintronics,[2] optical information processing,[3] and biological science.[4] The unique attribute of chiral photonics lies on the ability to manipulate the polarization of light and control the spin-mediated transition process.[5] Circularly polarized light (CPL), which can exhibit two possible polarization states (i.e., left- and right-handed circular polarizations), is an essential source of chiral photonics, in which the direction of the electric field rotates continuously in a plane perpendicular to the propagation direction with a steady angular velocity. This CPL interacts differently with different substances; therefore, the resulting change in polarization state can reveal the chemical configuration,[6] structural conformation,[7] and optoelectronic properties of a substance.[8] This chiroptical phenomenon and interpretation of chiral characteristics constitute the basis of chiral photonics. In particular, circularly polarized photoluminescence (CPPL) (i.e., differential emission of left-handed circularly polarized (LCP) and right-handed circularly polarized (RCP) lights) is absolutely necessary for scrutinizing the ground state of materials,[9] whereas circular dichroism (CD) spectroscopy (i.e., differential absorption of LCP and RCP lights) can provide useful information regarding the structure of the excited state of materials.[7] These complementary phenomena enable the development of advanced smart photonic technologies.

A material is chiral if it cannot be superimposed on its mirror image. This phenomenon is commonly observed in natural organic compounds, such as small amino acids, saccharide, starch, and DNA. Owing to their noncentrosymmetric structure (e.g., no inversion symmetry, mirror plane, and glide plane), chiral materials exhibit nonlinear optical responses to CPL in CD and CPPL spectra. Although organic chiral materials are ubiquitous and exhibit strong chiroptical activity in the near-UV region,[10] the structural softness of organic chiral molecules makes them difficult to stack, resulting in poor charge transfer capability in practical polarization-based optoelectronic devices. Additionally, in chiral photonics research, focus should be on stable and broad wavelength tunability over the visible light region to realize optoelectronic devices based on the polarization phenomenon. In this regard, OIHPs have emerged as promising candidates for nonlinear optic devices because of their facile color tunability through halide composition engineering,[11] quantum size effects,[12] small effective mass,[13] long spin lifetime exceeding 1 ns, diffusion lengths ≈85 nm, and high electron/hole mobility.[14] A recent study demonstrated that OIHPs exhibit strong spin–orbit coupling of the electronic states,[15] spin-dependent optical selection rules, and large Rashba splitting,[16] suggesting that the OIHPs might exhibit exceptional spin polarization properties.[17]

Despite the exceptional spin polarization properties, OIHP materials cannot be utilized in chiral photonics owing to their centrosymmetric crystal structure. However, the flexible crystal

S. Ma, Dr. J. Ahn, Prof. J. Moon
Department of Materials Science and Engineering
Yonsei University
50 Yonsei-ro Seodaemun-gu, Seoul 03722, Republic of Korea
E-mail: jmoon@yonsei.ac.kr

The ORCID identification number(s) for the author(s) of this article can be found under https://doi.org/10.1002/adma.202005760.

DOI: 10.1002/adma.202005760

structure of OIHPs breaks the inversion symmetry and enables new strategies for designing materials with desirable anisotropic properties. In 2003, Billing et al. first incorporated chiral ligands in the OIHP framework and reported the synthesis of 1D chiral perovskite single crystals.[18] A subsequent study in 2006 reported the synthesis of 2D chiral perovskite single crystals.[19] However, these noncentrosymmetric chiral perovskites were not utilized in chiral photonics until the breakthrough in 2017 when CD spectroscopy was first performed.[20] Since then, chiral perovskites have gained tremendous research attention in the chiral photonic community. However, only two review papers discuss the optical and electronic properties of chiral perovskites.[21] Therefore, in this review, we focus on theoretical fundamentals explaining the chiral transfer mechanism from optically active molecules to achiral materials. To explore the potential possibilities of these chiral photonic materials thoroughly, the fundamental basis of optical phenomena (i.e., CD and CPPL) needs to be clearly understood. The following sections discuss the recent development in chiral perovskite photonics based on the underlying chirality transfer mechanisms. Recent advance of chiral OIHPs based optoelectronic devices are also briefly discussed. Furthermore, this review suggests progressive perspectives and challenges that need to be addressed in this research area.

2. Fundamentals of Chiroptical Phenomena

2.1. Electric Transition and Transition Dipole Moment

Chiral photonics is based on the interaction between materials (e.g., atoms or molecules) and circularly polarized incident light. At longer wavelengths (>1000 nm), the interaction between the oscillating electromagnetic wave and atomic nuclei causes molecular vibration. However, for shorter wavelengths, the heavy nuclei cannot exhibit significant responses even when the surrounding electron cloud can be polarized according to the direction of the oscillating electric field. Such a redistribution of electrons results in an electronic transition from the ground state to the excited state. Based on this phenomenon, UV–vis absorption spectroscopy and CD spectroscopy can become powerful tools to obtain the electronic structural information of chiral materials. In organic chemistry, the absorption in a particular wavelength region is attributed to the electronic transition that is associated with a particular bond or structural unit. However, in chiral perovskite materials, the absorption in a particular wavelength region is generally related to the excitonic transition due to the low-dimensional quantum structure and large exciton binding energy.

The interaction between the electromagnetic wave (UV and visible region, 200–750 nm) and material can trigger the excitation of electrons from one state to another, resulting in a spatial redistribution of the net charge. Thus, an electric transition dipole moment (ETDM, μ) is induced by the incident electric field (**Figure 1**a, left). The yellow and green regions indicate the excited and ground states, respectively. The resulting ETDM designates the net linear displacement of charge during the transition. Furthermore, ETDM describes the polarization of the charge in the excited state and is completely different from the static dipole moment (or permanent dipole moment), which describes the polarization in the ground state based on the innate structure of a material. Therefore, ETDM has oscillating properties that depend on the phase of wave functions. ETDM is a complex vector quantity, where the initial point of the vector is located at the center of gravity of the material, and its direction represents the polarization of the transition.[22]

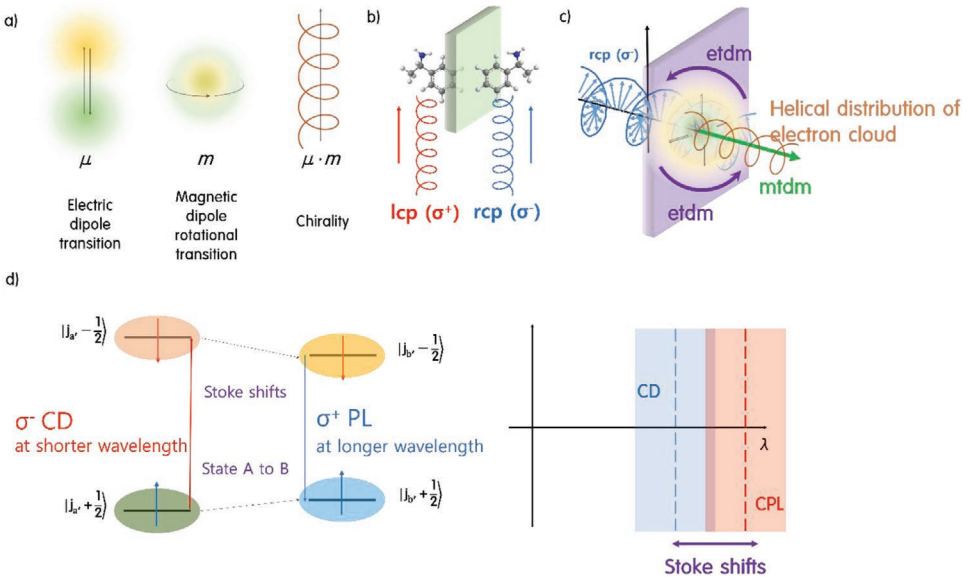

Figure 1. Fundamentals of electronic transition and chiroptical phenomena. a) Schematic of electric dipole transition by linear force (left), magnetic dipole transition by rotational Lorentz force (middle), and chirality as a result of the dot product of electric and magnetic transitions (right). b) Illustration of chiral materials exhibiting different absorption behavior with LCP (σ^+) and RCP (σ–) lights. c) Evolution of helical distribution of electron cloud due to the interaction between ETDM and MTDM. d) Schematics describing the chiroptical phenomena (CD and CPPL) based on the electronic transition and Stokes shift.

The square of the ETDM is proportional to the intensity of electronic transition, which reflects the manner in which the material will interact with an incident electromagnetic wave in a given polarization state. For instance, if the dipole transition is forbidden, $\mu = 0$, whereas $\mu > 0$ when the transition is allowed. An oscillating electric field generates an oscillating magnetic field. Thus, a magnetic dipole transition moment (MTDM, m) can also be defined as the net circulation of charge for each electric transition (Figure 1a, middle).[22] Generally, in achiral materials, the square of ETDM tends to be five orders of magnitude larger than the square of MTDM. Therefore, ETDM is a determinant factor in optical spectroscopy, such as UV–vis absorption spectroscopy. However, this situation does not apply to chiral materials because chiral photonics is based on the interaction between ETDM and MTDM (Figure 1a, right).

2.2. Chiroptical Activity

2.2.1. Circular Dichroism

In chiral photonics, as the incident lights of LCP (σ^+) and RCP (σ^-) are chiral, they interact differently with a material when electronically excited by specific excitonic transitions (Figure 1b). For instance, chiral perovskites preferentially absorb LCP or RCP light based on the redistribution of helical electron clouds for a particular transition. This differential absorption of LCP and RCP lights is often referred to as the Cotton effect or CD intensity (ΔA), which is defined as follows:

$$\Delta A = A^{\mathrm{L}} - A^{\mathrm{R}} \tag{1}$$

where A^{L} and A^{R} are the absorbance of LCP and RCP lights, respectively. The CD spectrum provides important information about the configuration of materials and properties of electronic transitions.[23]

To gain in-depth knowledge of why chiral materials preferentially absorb LCP or RCP light, it is necessary to understand how light absorption is determined in terms of transition dipole moments. As mentioned previously, the incident light (LCP or RCP light) in chiral photonics has a constant magnitude as the direction rotates at a constant rate (blue line in **Figure 2**b). The polarized incident light can induce a displacement of electronic charge at each point along the direction of rotation of incident light, thus creating an ETDM ($\mu_{\mathrm{net}} \neq 0$). As the incident light propagates into the chiral materials (e.g., the absence of mirror plane or center of symmetry), the resulting electronic transition can accompany a circulation of charge, thereby creating

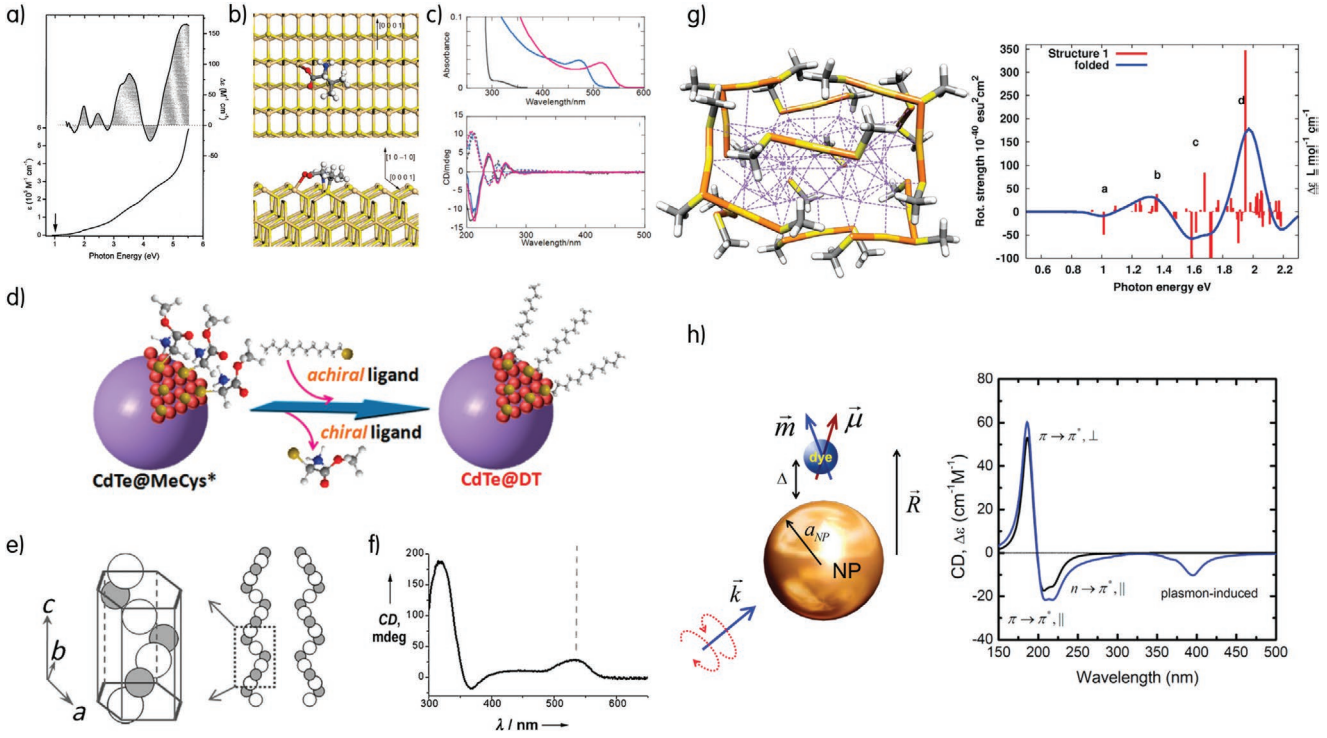

Figure 2. Chirality transfer mechanism in inorganic QDs or metallic NPs compounds induced by chiral surface distortion. a) CD spectrum and optical absorption spectra (lower) for gold-glutathione cluster compound. Reproduced with permission.[27] Copyright 2000, American Chemical Society. b) Top and side views of the proposed bonding of D-penicillamine to the surface of wurtzite. Reproduced with permission.[29] Copyright 2008, American Chemical Society. c) UV–vis absorption spectra (upper) and CD spectra (lower) of D-MeCys-capped CdS (black), CdSe (blue), and CdTe (red) NCs. d) Schematic of ligand exchange reaction. Reproduced with permission.[30] Copyright 2009, American Chemical Society. e) Schematic of opposite spiral of atoms, and f) CD spectrum of HgS NCs in the range of 450–600 nm. Reproduced with permission.[31a] Copyright 2013, Wiley-VCH. g) Optimal atomic distribution of Au_{38} cluster (left) and calculated rotatory strength and CD spectrum of Au_{38} cluster. Reproduced with permission.[33c] Copyright 2010, American Chemical Society. h) Schematic of a complex composed of a metal NP and chiral dye molecule (left). Calculated CD signals (right) for the α-helix (black line) and complex (blue line). Reproduced with permission.[6b] Copyright 2010, American Chemical Society.

an MTDM, which results in a helical redistribution of the electron cloud, as shown in Figure 1c. As this redistribution can be induced by LCP or RCP light in chiral photonics and chiroptical spectroscopy (e.g., CD and CPPL), the transitions in which both transition dipole moments are induced simultaneously can be detected.

Theoretically, the absorption of LCP or RCP light occurs when the scalar product of two dipole transition moments has a nonzero value. The integral of the CD spectrum (i.e., the degree of light absorption) is directly proportional to the scalar product defined as the rotational strength R_{ab}.

$$\int \Delta\varepsilon \, \mathrm{d}\nu \propto R_{ab} \approx |\mu_{ab}| |m_{ab}| \cdot \cos\theta \tag{2}$$

where R_{ab} describes the electronic transition from state A to state B, $\Delta\varepsilon$ and θ are the difference of extinction coefficient between LCP and RCP lights and angle between ETDM and MTDM, respectively. Rotational strength is a signed quantity whose sign varies according to θ. Therefore, R_{ab} for mirror image arrangements (i.e., *S*- or *R*-configuration in chiral molecules) was predicted to have an equal absolute magnitude but an opposite sign. Furthermore, a general rule in CD spectroscopy states that the integral of CD over the entire wavelength region is zero. According to this sum rule, if a positive CD band exists in a spectral region, there are necessarily one or more bands of negative sign elsewhere.[6a]

2.2.2. Circularly Polarized Photoluminescence

CPPL spectroscopy relies on the differential spontaneous emission of LCP or RCP light from luminescent systems. This difference is defined by the expression given by Equation (3), which is similar to Equation (1).

$$\Delta I = I^{L} - I^{R} \tag{3}$$

where I^{L} and I^{R} are luminescence intensities of LCP and RCP lights, respectively. As CPPL and CD are based on opposite optical phenomena (i.e., emission and absorption of light), the CD spectrum reflects the structural properties of the excited state, whereas CPPL provides information of ground states.[22] However, CPPL and CD can be explained in terms of the same quantum mechanical parameter and rotational strength R_{ab}, which determines whether the transition is allowed or forbidden.[24] The degree of CPPL is generally reported in terms of the luminescence dissymmetry ratio, g_{lum}.

$$g_{lum} = \frac{2 \times \left(I^{L} - I^{R}\right)}{\left(I^{L} + I^{R}\right)} \tag{4}$$

To generate CPPL, the light absorption must be first realized, followed by energy transfer or decay process to luminescent state within a time scale of spin flip (Figure 1d). As the CPPL is the last to occur among several sequential optical phenomena, the materials exhibiting CPPL are relatively rare compared with those exhibiting CD, as shown in Figure 1d. Energy transfer and Stokes shift are nonradiative energy loss processes; thus, the wavelength region where CPPL is observed is longer than that of CD. Furthermore, efficient spin and energy funneling have been reported in low-dimensional chiral perovskites with high CPPL quantum yields because of their long spin lifetime that exceeds 1 ns and exceptionally long spin-diffusion length of ≈85 nm.[25]

3. Chirality Transfer Mechanism

As organic and biological molecules or complexes that exhibit strong chiroptical activity are abundant in nature (e.g., amino acids, saccharide, starch, and DNA), the theoretical fundamentals of chiroptical phenomena are based on structural organic chemistry, which primarily deals with small chromophores. Small chromophores comprise functional groups or a combination (or coupling) of several functional groups resulting in one or more chiroptical responses in the UV and visible light range. However, it is difficult to use chiral organic molecules in chiral photonics or optoelectronic devices based on polarization phenomena because of their structural softness and poor electrical properties. Recently, it was discovered that the chirality of the molecular moiety can be easily transferred to achiral building blocks (e.g., inorganic semiconductors and metallic compounds).[26] The higher carrier mobility and exceptional absorption or emission properties in the visible region for achiral building blocks can compensate for the limitations of the chiral organic moiety. Therefore, assembling hybrid materials composed of achiral crystalline materials and chiral organic molecules has been recognized as an ideal strategy to achieve a synergy for strong chiroptical activity. Additionally, this assembly strategy utilizes a familiar organic moiety possessing the chromophores as building block (i.e., benzene, styrene, naphthalene, and cyclohexane). Therefore, the prior knowledge and fundamental basis of structural organic chemistry (mentioned in Section 2) can be applied to scrutinize the chiroptical properties of hybrid materials. Recent studies have reported that chirality transfer from optically active chiral organic moieties to achiral building blocks can originate from several well-defined phenomena, such as i) chiral distortion of the surface induced by chiral molecules, ii) chiral molecules mediated crystallization into a chiral structure, iii) supramolecular chiral self-assembly, and iv) electronic interactions between chiral molecules and achiral building blocks.

3.1. Chiral Molecule-Induced Surface Distortion

As the adsorption or interaction between chiral molecules and achiral materials primarily occurs at the surface of achiral materials during synthesis, it is reasonable to assume that the deformation of the surface structure could induce chirality transfer from chiral molecules to achiral substances. Striking chiral transfer from chiral capping molecules (l-glutathione) to inorganic gold cores was first demonstrated by Schaaff and Whetten.[27] They observed the strong chiroptical activity in the metal-based electronic transition across the near-UV, visible, and near-IR regions (Figure 2a). This broad wavelength region (from near-UV to near-IR) and strong chiroptical

responses of cluster compounds suggested that the electronic structure of the metal is easily tunable by the adsorbed glutathione capping molecules. The experimental results were supported by the theoretical explanation in 2006 even when the core is inherently achiral, the chiroptical properties can be imposed on clusters by chiral adsorbates.[28] This triggered follow-up studies on chiral hybrid systems composed of chiral molecules with achiral metal nanoparticles (NPs) or semiconductor nanocrystals (NCs). The studies conducted by Gun'ko et al.[29] (Figure 2b) and Kawai et al.[30] (Figure 2c,d) successfully verified that chiral surface distortion can induce chiroptical activity in hybrid materials even when the core continues to be achiral.

3.2. Chiral Structure Mediated by Chiral Molecules

Although the chiral transfer mechanism by surface distortion is fully supported by experimental evidence[30] and theoretical calculations,[28,29] the induced chiroptical effect is limited to exhibiting low values in the CD spectra, as shown in Figure 2c.[30] Based on this perspective, the crystallization process of chiral materials and various inherent chiral inorganic crystals (i.e., quartz, α-HgS, β-AgSe, tellurium, and selenium) has attracted extensive research interest owing to their chiroptical properties, which are similar to those of bulk single crystals.[31] Chiral crystals can be classified into 65 different Sohncke space groups capable of exhibiting chiroptical responses and exhibiting ferroelectric properties based on the Neumann–Curie principle.[32] In 2013, Ben-Moshe et al. reported a direct phase transition from the achiral phase of β-HgS to a chiral phase of α-HgS (Figure 2e) with a strong chiroptical response using a chiral molecule (penicillamine).[30a] As shown in Figure 2f, the chiroptical effect of the obtained α-HgS NCs revealed several orders of magnitude (≈200 mdeg) higher than that of previously reported chiral quantum dots (QDs) (e.g., CdS, CdSe, and CdTe in Figure 2a,c) induced by chiral surface distortion.[27–30] This strong signal suggests that the chiroptical activity is attributed to the chiral crystal structure rather than the chiral surface distortion mechanism.

3.3. Supramolecular Chiral Self-Assembly

In addition to possessing the inherent chiral crystal structure, metallic compounds could exhibit a chirality through the supramolecular chiral self-assembly on a macroscopic scale when their synthesis conditions are varied.[33] Although the metallic constituents are achiral, the resulting nanoclusters such as Au_{102}(*p*-MBA)$_{44}$ (*p*-MBA: *para*-mercaptobenzoic acid) and $Au_{38}(SR)_{24}$ (SR: thiolate) exhibit prominent chiroptical responses as shown in Figure 2g.[33] The induction of chirality is attributed to the organization of staple motifs in surface of self-assembled clusters, which form chiral patterns. In this regard, shape or morphology on a macroscopic scale also significantly affects the chiroptical activity response of chiral materials in the visible wavelength region. Therefore, the morphology of materials should be also considered as a determinant factor for chiroptical applications.[34]

3.4. Electronic Interaction between Chiral and Achiral Systems

The chirality from chiral organic molecules to achiral semiconductor QDs or metallic NPs can be easily transferred via the spatial rearrangement of atoms in an achiral system (e.g., chiral surface distortion, induced chiral crystal structure, and inherent chiral crystal structure) and supramolecular self-assembly. However, chiroptical properties can be obtained even when the atomic arrangement of the bulk or surface remains achiral. The last chiral transfer mechanism is based on the electronic interaction[35] or coupling phenomenon[36] between chiral molecules and achiral semiconductor or metallic compounds.[37]

As shown in Figure 2h, based on theoretical calculations, Govorov et al. first anticipated that achiral NCs can exhibit active CD signals when the excitations of achiral NPs (e.g., metal or inorganic semiconductor NCs) are coupled with the molecular excitation of chiral molecules.[6b] Although NPs themselves are not chiral and cannot exhibit CD signals, the CD signal at the plasmon frequency (approximately 400 nm) appears as a consequence of the exciton–plasmon interaction (Figure 2h, right panel). In other words, the oscillating dipole of a chiral molecule can induce dissipative chiral currents in metallic NPs even if the atomic arrangement of NPs remains achiral. These results demonstrate that chirality transfer can be easily realized by Coulomb interaction between adjacent dipole electronic transitions, implying that the strong adsorption of chiral molecules at the surface is not essential.

4. Chiral Perovskites

For a hybrid system comprising achiral materials and chiral organic molecules, the chirality of small or large organic molecules can be transferred through either the spatial re-distribution of atoms (e.g., mechanism (i) and (ii) in Sections 3.1 and 3.2), or the electric interaction between the chiral and achiral systems (mechanism (iii) in Section 3.4). Owing to the exceptional optoelectronic properties of OIHPs, such as high absorption coefficient, low non-radiative recombination rate, high photoluminescence quantum yield, and long carrier lifetime, numerous studies have explored OIHPs as achiral platforms for chiral photonics and spin-based optoelectronic applications. Despite substantial progress, the origin of induced chirality or chirality transfer mechanism in perovskites is still ambiguous. Classifying recent works in terms of underlying different chiral transfer mechanisms, as observed in chiral semiconductor QDs and chiral metal NPs, can shed light on developing effective strategies to further improve chiroptical activity and in designing practical optoelectronic devices.

4.1. Chiral Surface Distortion of Chiral OIHPs

Chiral surface distortion, which is caused by the interaction between chiral organic molecules or capping agents and surface of core materials (e.g., QDs or metal NPs), has been observed in chiral OIHPs. In 2017, the chiral perovskite NCs ($CsPb(I/Br)_3$) decorated with a chiral ligand (enantiomeric 1,2-diaminocyclohexane, DACH) was first reported. $CsPb(I/Br)_3$ NCs capped

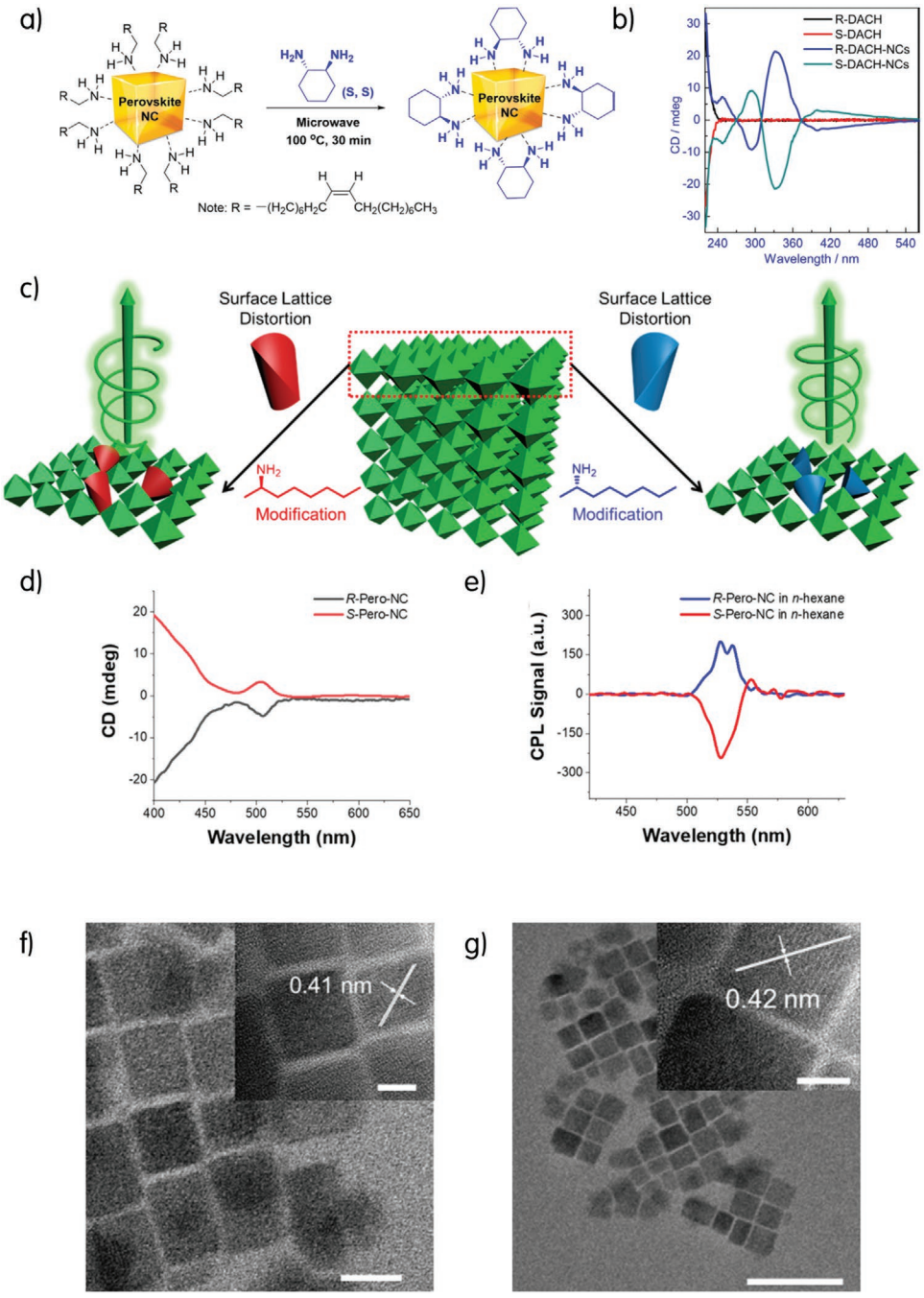

Figure 3. Chirality transfer in OIHPs induced by chiral surface distortion. a) Ligand exchange of OA-capped perovskite NCs using pure enantiomers of DACH. b) CD spectra of low concentration DACH and perovskite NCs stabilized with a small amount of DACH. Reproduced with permission.[38] Copyright 2017, AIP Publishing. c) Schematic of chirality induction mechanism by surface lattice distortion. d) Electronic CD of prepared chiral perovskite NCs and e) one-photon CPPL spectra of chiral perovskite NCs dispersed in *n*-hexane. TEM images of f) prepared *S*-perovskite NCs and g) rac-perovskite NCs. Reproduced with permission.[39] Copyright 2019, American Chemical Society.

with oleylamine (OA) were added to a mixture of chiral DACH and *n*-hexane[38] [1*R*, 2*R*- or 1*S*, 2*S*-DACH, and $CsPb(I/Br)_3$] and then exposed to microwave irradiation (**Figure 3**a), which led to the spontaneous ligand exchange from an achiral capping agent (OA) to a chiral stabilizer (1R, 2R- or 1S, 2S-DACH). As shown in Figure 3b, the resulting chiral NCs (*R*- or *S*-DACH-NCs) clearly exhibited chiroptical activity in the CD spectrum. *R*-DACH-NCs displayed two negative Cotton effects at 290 nm and 400 nm along with a positive CD signal at 333 nm (blue line in Figure 3b). In contrast, the CD spectrum of pure *R*-DACH only revealed a positive Cotton effect at a shorter wavelength of 233 nm (black line in Figure 3b). This confirmed that the Cotton effect represented by *R*-DACH-NCs did not originate from the pure chiral stabilizer, but from the chirality of NCs,

which was transferred from the stabilizer. Interestingly, the chiroptical activity of $CsPb(I/Br)_3$ NCs remained unchanged even after the removal of chiral molecules, which was also observed in chiral CdX NCs (X = S, Se, and Te).

Chen et al. also synthesized inorganic colloidal NCs of chiral $CsPbBr_3$ via a typical in-situ process (i.e., direct growth of perovskite NCs in the presence of precursor and chiral molecules) in which *R*- or *S*-α-octylamine was utilized as the chiral capping ligand (Figure 3c).[39] In addition to the CD spectra, CPPL spectroscopy was also used to examine the chiroptical activity of chiral NCs. As shown in Figure 3d, the mirror image of the signal was obtained in the CD spectra at 504 nm. However, the CPPL signals of chiral NCs were detected above 525 nm (Figure 3e) and were slightly red-shifted compared with the CD signal. Because the time scale of spin-flip is extremely short and the quantum confinement effect of NCs is strong, as mentioned in Section 2.2.2, the mirror image of the CD signal could be assigned to the exciton transition of NCs, which originates from the interaction between the chiral capping ligand and NC surface. The excess bromide atoms on the NC surface promoted selective chiral amine binding with Br-rich defect sites, resulting in a distorted surface pattern of NCs (Figure 3c). High-resolution transmission electron microscopy (HRTEM) images of NCs capped with *S*-α-octylamine (Figure 3f) and racemic α-octylamine (Figure 3g) exhibited no structural difference. Additionally, HRTEM demonstrated that all $CsPbBr_3$ NC cores were centrosymmetric. Therefore, they could not exhibit chiroptical responses. The synthesized chiral $CsPbBr_3$ NCs exhibited a similar magnitude of CD intensity and luminescence dissymmetry ratio (g_{lum}) as those of the hybrid materials (i.e., chiral inorganic QDs and chiral metal NPs) discussed in Section 3.1.[40] This suggests that the chirality transfer mechanism via surface distortion in semiconductor or metal NCs could also be applied to chiral OIHP systems. Consequently, an in-depth study of ligand chemistry or ligand engineering, similar to that performed on QDs and metal NP systems,[41] could play a key role in determining the chiroptical activity of chiral OIHPs.

4.2. Inherent Chiral Crystal Structured OIHPs Involving Chiral Molecules

As described in Section 3.2, chirality can be effectively transferred from chiral organic molecules to achiral QDs and metal NPs via chiral molecule-mediated chiral structure induction mechanism (i.e., the transition of chiral crystal structure and chiral shape). However, owing to the structural stiffness of QDs and metal NPs, chiral ligands are unable to directly intercalate into the lattice of achiral crystals, and thus, only modifying the atomic arrangement. In contrast, owing to the structural flexibility of OIHPs,[42] chiral molecules can directly penetrate into the perovskite lattice and form inherent chiral crystal structures. Therefore, inherent chiral crystal-structured OIHPs incorporating chiral molecules are expected to exhibit a stronger chiroptical effect than that of induced chiral structured QDs and metal NPs.

Lead-based chiral perovskites (e.g., PbX_3R, PbX_4R_2, and $PbX_5R_3 \cdot H_2O$; X = halide ion, R = aromatic amine) with chiral organic molecules incorporated into the layered lead iodide framework was first reported by Billing and Lemmerer.[18,19] Although the crystalline structure of chiral perovskites belonged to the chiral space group of $P2_12_12_1$ (**Figure 4**a), their chiroptical properties were explored by Ahn et al..[20] In this pioneering study, Ahn et al. adopted small chiral molecules of *R*- and *S*-methylbenzylamine (*R*- and *S*-MBA), which were intercalated into the layered lead iodide framework to obtain chiral perovskite $(R\text{-MBA})_2PbI_4$ and $(S\text{-MBA})_2PbI_4$ thin films. As *R*- and *S*-MBA molecules had a size and molecular structure (aromatic structure) similar to those of the aromatic amine organic cations used by Billing et al. in his previous work, the resulting chiral perovskite was crystallized to exhibit the same chiral space group of $P2_12_12_1$. The CD spectra of $(R\text{-MBA})_2PbI_4$ and $(S\text{-MBA})_2PbI_4$, as depicted in Figure 4b, exhibited a clear bisignate signal at 489 and 501 nm, which were near the first excitonic transition of perovskite (497 nm). The cross point for the positive and negative Cotton effects are located exactly at the wavelength where the first excitonic transition of OIHPs occurs. However, when a racemic mixture of MBA (rac-MBA) was used, the resulting perovskite, $(\text{rac-MBA})_2PbI_4$, retained an inversion and mirror plane symmetry element with the nonchiral space group $P2_1/a$ without exhibiting any optical activity in the CD spectra. As the racemic compound mixture contains an equal amount of *R*- and *S*-configuration molecules, the chirality transfer occurs during the controlled crystallization, thereby promoting the entire structure or shape of OIHPs to assemble into an inherent chiral structure accompanied by twisted perovskite unit cells. As a result, the net rotational strength is non-zero in $(R\text{-MBA})_2PbI_4$ and $(S\text{-MBA})_2PbI_4$ (which may have an oblique configuration of ETDM and MTDM, respectively), thus exhibiting a Cotton effect in the CD spectra at different wavelengths. The degree and appearance of the Cotton effect in thin films can be varied by controlling crystallization kinetics. Because the CD signal of chiral OIHPs strongly depends on the morphology and orientation of thin films (Figure 4c,d), which are significantly influenced by the synthesis conditions (e.g., addition of cosolvent (dimethyl sulfoxide), precursor concentration, and amount of chiral molecules), morphology, shape, and crystal quality of chiral perovskites, are also determinant factors that enhance the chiroptical properties.

Inspired by this work, Long et al. reported that the degree of spin polarization can be controlled by tuning the chiral ligand composition and magnetic field.[42] Owing to the flexible crystal structure and ionic composition of quasi-2D (also known as Ruddlesden-Popper) perovskites, the composition ratio of chiral cations is easily tunable. The pure chiral 2D perovskite of *R*- or $S\text{-}(MBA)_2PbBr_4$ ($\langle n \rangle = 1$, where $\langle n \rangle$ is the average number of inorganic layers between chiral organic molecules) was first synthesized by incorporating *R*- or *S*-MBA-Br. The chiral 2D perovskite with $\langle n \rangle = 1$ is expected to exhibit the strongest chiroptical activity because it contains the largest molecular fraction of the chiral ligand with respect to the achiral inorganic framework (e.g., $PbBr_4$). However, CPPL emission was not observed for the pure 2D chiral perovskite, and this was attributed to the very poor photoluminescence quantum yields (PLQYs) due to significant non-radiative recombination. Increasing the dimension of quasi-2D perovskites (i.e., $\langle n \rangle$ value) could promote efficient energy funneling and exciton

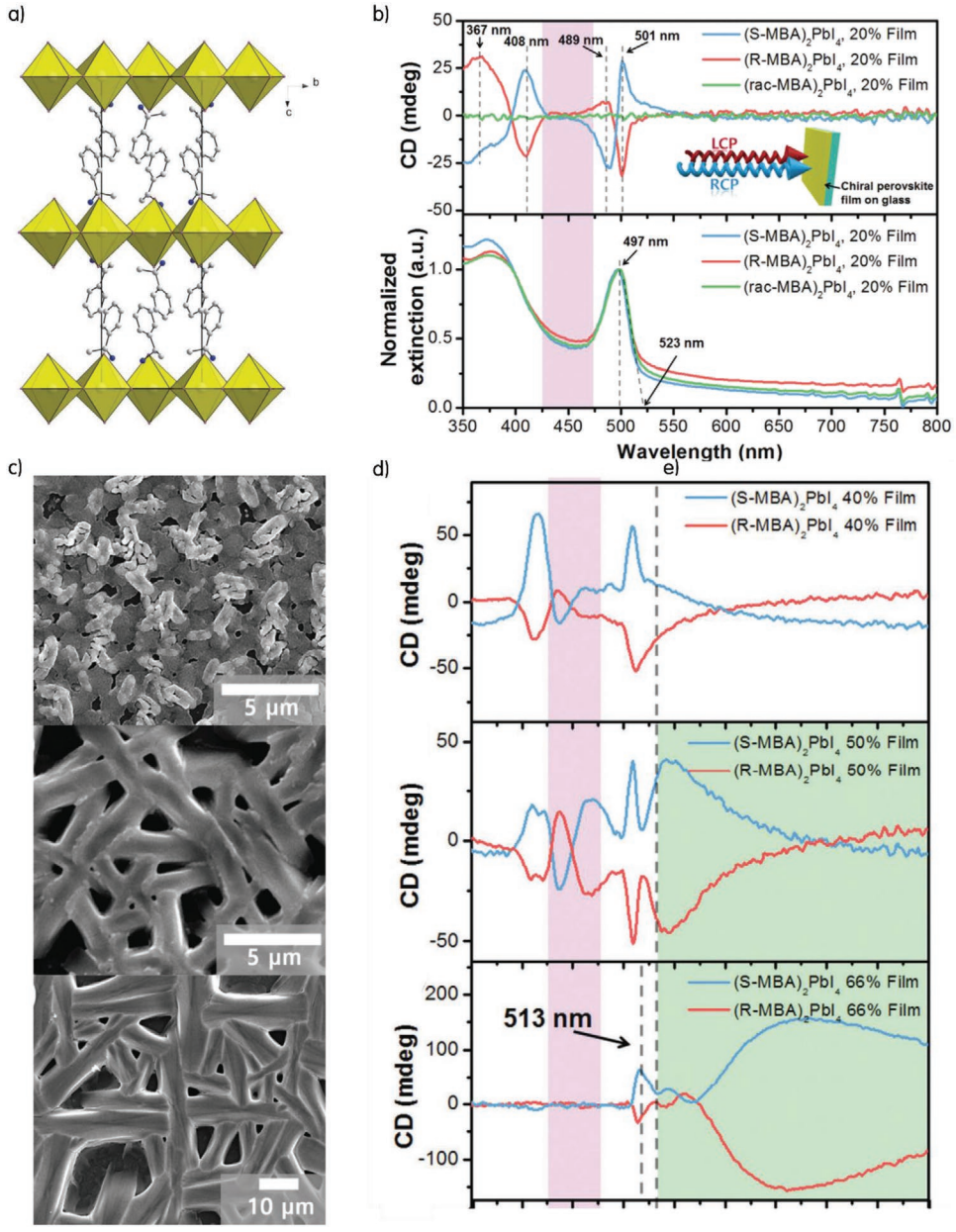

Figure 4. Chirality transfer in OIHPs induced by their inherent chiral structure. a) Schematic of chiral crystal structure of hybrid PbI_4R_2 system. Reproduced with permission.[19] Copyright 2006, Royal Society of Chemistry. b) Transmission CD spectra of chiral perovskite films with the chiral space group $P2_12_12_1$. c) SEM image of $(R\text{-MBA})_2PbI_4$ films fabricated using different concentration solutions (upper: 40 wt%, middle: 50 wt%, lower: 66 wt%). d) Transmission CD spectra of (R- and S-MBA)$_2PbI_4$ films formed using different solution concentrations. Reproduced with permission.[20] Copyright 2017, Royal Society of Chemistry.

transfer. Therefore, to obtain efficient photoluminescence emission, the compositional ratio of chiral ligands needs to be decreased. The CD signal around 400 nm decreased gradually from pure 2D perovskite with $\langle n \rangle = 1$ to quasi-2D perovskite with $\langle n \rangle = 3$, and then completely disappeared for the quasi-2D perovskite with $\langle n \rangle = 5$. However, the CD signal of chiral ligands (R- or S-MBA-Br) only reveals the Cotton effect at wavelengths shorter than 270 nm. Furthermore, the Cotton effect of quasi-2D perovskites was confirmed to originate from their chirality because of their inherent chiral structure. As the energy funneling and chirality transfer are oppositely influenced by the chiral ligand composition ratio, the dimensions of quasi-2D perovskites should be carefully determined. While considering the chirality transfer and energy funneling process, highly efficient CPPL (up to 3%) was achieved for chiral $\langle n \rangle = 2$ quasi-2D perovskite without applying any external magnetic field. Compared with the 3D achiral perovskite, where the same degree of polarization is obtained only under an external magnetic field of 5 T, this multifunctional quasi-2D chiral perovskite has unprecedented potential in chiral photonics.

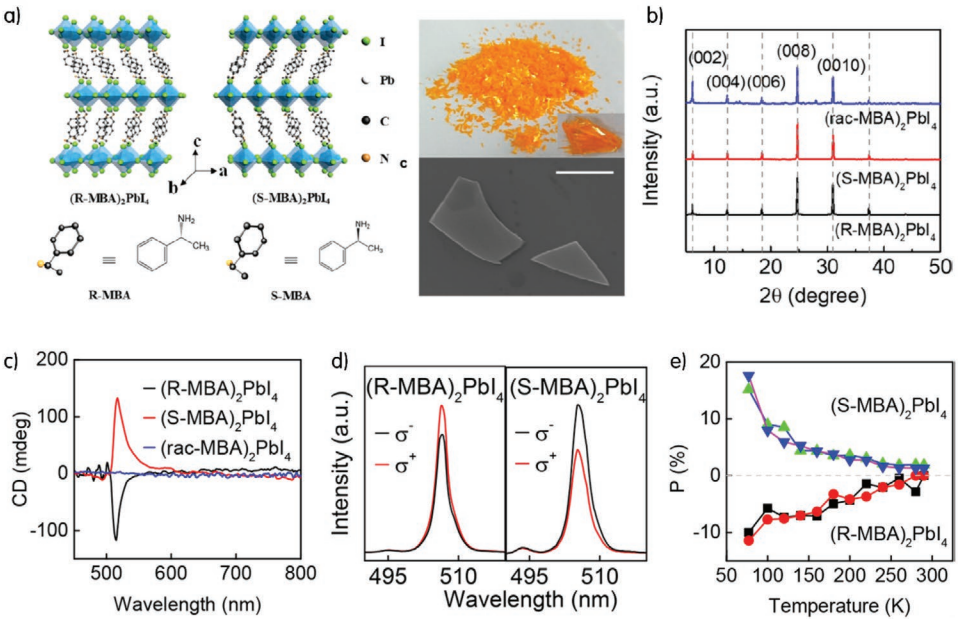

Figure 5. Chirality transfer in OIHPs induced by the inherent chiral structure. a) The crystal structure of pure chiral 2D OIHPs, optical microscopy image, and SEM images of (*R*-MBA)$_2$PbI$_4$. b) XRD patterns of as-synthesized (*R*-MBA)$_2$PbI$_4$, (*S*-MBA)$_2$PbI$_4$, and (rac-MBA)$_2$PbI$_4$. c) CD spectra and d) CPPL spectra of (*R*-MBA)$_2$PbI$_4$, (*S*-MBA)$_2$PbI$_4$, and (rac-MBA)$_2$PbI$_4$. e) Degree of CPPL as a function of temperature. Reproduced with permission.[43] Copyright 2019, American Chemical Society.

Recently, Ma et al. synthesized the same chiral 2D perovskites [(*R*-MBA)$_2$PbI$_4$ and (*S*-MBA)$_2$PbI$_4$] via a solution method (**Figure 5**a).[43] The X-ray diffraction (XRD) patterns of the resulting crystals had a very narrow full-width at half maximum, which suggests the excellent crystal quality of the synthesized chiral perovskites (Figure 5b). Moreover, the spin-coated films of (*R*-MBA)$_2$PbI$_4$ and (*S*-MBA)$_2$PbI$_4$ on quartz substrates exhibited strong CD signals of over –100 and 100 mdeg, respectively (Figure 5c). Compared with the amplitude of the previously reported Cotton effect, the strong CD signals stems from the excellent crystal quality and well-aligned orientation, as confirmed by XRD. Furthermore, the strong CD signal suggests a well-defined electronic band state of chiral perovskite; thus, the high-quality chiral 2D perovskites are expected to display enhanced CPPL. Therefore, to examine the CPPL characteristics of chiral OIHPs, polarization sensitive photoluminescence analysis was performed for as-exfoliated perovskite microplates at 77 K. As expected, an evident intensity difference of CPPL was clearly observed between LCP (σ^+) and RCP ($\sigma-$) at ≈505 nm, as shown in Figure 5d. To quantify the degree of CPPL, the luminescence dissymmetry ratio, g_{lum}, was calculated for more than 16 microplates, and the average g_{lum} of (*R*-MBA)$_2$PbI$_4$ and (*S*-MBA)$_2$PbI$_4$ were 9.6% and 10.1%, respectively. To unveil the origin of the considerably enhanced chiroptical properties of chiral perovskites, temperature-dependent CPPL measurements were obtained in the range from 77 to 290 K. As shown in Figure 5e, the g_{lum} value decreased gradually with increasing temperature and finally became zero at room temperature. With increasing temperature, the enhanced phonon–electron interaction and thermal vibration of the lattice could relax the lattice distortion, and thus, reduce the chirality of OIHPs.[44] The reduced spin-flip time could also be a reason for the decreasing CPPL intensity difference with increasing temperature.[15]

In addition to the chiral perovskite with the chemical formula PbX_4R_2 (i.e., *R*- and *S*-MBA$_2$PbI$_4$ or MBA$_2$PbBr$_4$), the chiroptical properties of PbX_3R and its CPL detection application have also been reported.[45] While the chiral organic molecule α-phenylethylamine (PEA) was utilized as the A-site cation, a single crystal of (*R*- and *S*-α-PEA)PbI$_3$ was first synthesized by the inverse temperature crystallization method. The XRD analysis revealed that the single crystal adopts a 1D structure of face sharing $(PbI_6)^{4-}$ octahedral surrounded by chiral α-PEA$^+$ cations. However, the (*R*- and *S*-α-PEA)PbI$_3$ single crystal has only twofold screw symmetry. Thus, the chiral space group is $P2_12_12_1$ in an orthorhombic crystal system.[19] To examine the chiroptical properties of (*R*- and *S*-α-PEA)PbI$_3$, the presynthesized single crystal was redissolved in dimethylformamide to obtain highly oriented high-quality films using the spin-coating method. Irrespective of the *R*- or *S*-configuration, all the films exhibited strong excitonic extinction at 374 nm. Both (*R*- and *S*-α-PEA)PbI$_3$ films showed strong CD signals, whereas the racemic mixture film did not exhibit an optical response in the CD spectra. Because the peaks of the CD signal in (*R*- and *S*-α-PEA)PbI$_3$ films (328 nm and 392 nm, respectively) were located significantly far from the CD position for a single α-PEA molecule (259 nm), the chirality of (*R*- and *S*-α-PEA)PbI$_3$ films came from the inherent chiral crystal structure (space group of $P2_12_12_1$) involving chiral molecules.

Recently, Ahn et al. investigated the crystalline phase transition-dependent changes in the CD signal by varying the composition of halide ions to demonstrate that the chirality of OIHPs is attributed to the inherent chiral crystal structure.[46] As shown in **Figure 6**a, the crystal structure transition occurs

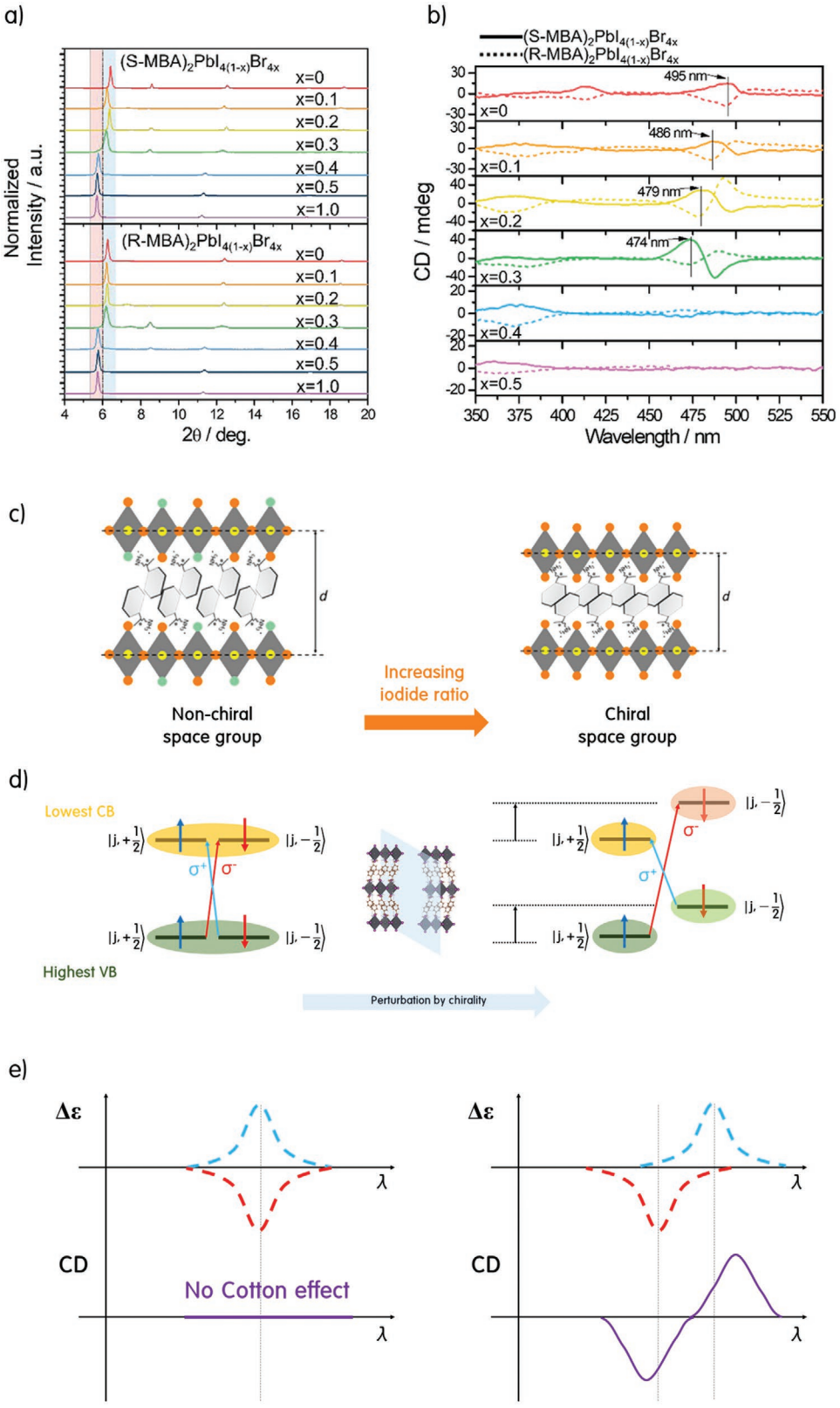

Figure 6. Origin of chirality in OIHPs. a) XRD patterns of $(R\text{-MBA})_2PbI_{4(1-x)}Br_{4x}$ and $(S\text{-MBA})_2PbI_{4(1-x)}Br_{4x}$ ($x = 0$, 0.1, 0.2, 0.3, 0.4, 0.5, and 1.0). b) CD spectra of $(R\text{-MBA})_2PbI_{4(1-x)}Br_{4x}$ and $(S\text{-MBA})_2PbI_{4(1-x)}Br_{4x}$ ($x = 0$, 0.1, 0.2, 0.3, 0.4, and 0.5). Reproduced with permission.[46] Copyright 2020, American Chemical Society. Schematic of c) phase transition and d) centrosymmetry breaking (or degeneracy breaking) in chiral OIHPs. e) Schematics explaining the origin of Cotton effect.

abruptly when the bromide ratio exceeds $x = 0.4$, accompanied by the sudden disappearance of the Cotton effect (Figure 6b). The anion substitution (i.e., iodide to bromide) causes the rotation of organic chiral molecules (e.g., *R*- or *S*-MBA cations) and tilting in the lead halide lattice. Both cation rotation and lattice tilting induce structural changes from the chiral space group of iodide-determinant phase to the achiral space group of bromide-determinant phase. Based on these findings, the origin of the asymmetric CD spectra observed in chiral OIHPs could be understood in terms of their quantum mechanical aspect. In the bromide-determinant phase (i.e., nonchiral space group in Figure 6c), the energy states are degenerate. Moreover, there is no difference between the required photon energies for absorbing LCP and RCP light, resulting in the absence of the CD signal. However, as bromide anions are replaced by iodide anions, OIHPs undergo a crystal phase transition to the iodide-determinant phase (i.e., chiral space group in Figure 6c). As the resulting iodide-determinant phase belongs to the chiral space group ($P2_12_12_1$), the permissible excitonic states can be altered through slight perturbation by the chirality of OIHPs (Figure 6d). Therefore, the degeneracy of energy states (same total angular moment quantum number *j*, but different magnetic quantum number m_s) is broken. This means that the energy state with the down spin $|j,-\frac{1}{2}\rangle$ is no longer similar to the energy state with the up spin $|j,+\frac{1}{2}\rangle$.[42,46] Therefore, the required photon energy for LCP and RCP light absorption is different, and this produces CD signals in different wavelength regions (Figure 6e).

According to the aforementioned studies, stronger chiroptical activity can be induced by inherent chiral crystal structures of OIHPs (g-factor over 6×10^{-3})[43] than that induced by other mechanisms (g-factor of about 3×10^{-3}) (chiral surface distortion induced mechanism and induced chiral structure mechanism) due to the higher compositional ratio of chiral organic molecules. Owing to the flexibility of the crystal structure of low-dimensional OIHPs, various chiral organic molecules, such as 1-(1-naphthyl)ethylammonium,[46] β-methylphenethylammonium,[47] and 1-(4-chlorophenyl)-ethylammonium,[48] cyclohexylethylammonium[49] can be utilized as chiral spacers between the corner-sharing octahedral layers apart from MBA and α-PEA chiral molecules. For example, chloride-based 2D chiral OIHPs with *R*-(-)-3-aminopiperidine or *S*-(+)-3-aminopiperidine chiral ligands have been reported. Furthermore, the chirality of this material is derived from the unusual distorted pentagonal pyramid geometry of the Pb(II) atom.[50] Thus, numerous combinations of chiral perovskites are possible, and further optimization processes are necessary to obtain high-quality well-aligned crystal structures along the chiral axis.[51]

4.3. Electronic Interaction between the Chiral Molecules and Achiral Platform of OIHPs

Although the chirality of most reported chiral OIHPs originate from the inherent chiral crystal structure (mechanism (ii) in Section 4.2), there is another highly plausible chirality transfer mechanism. The chirality transfer from chiral organic molecules to achiral OIHPs can be interpreted as the Coulomb dipole–dipole interaction. Recently, several reports suggested that this Coulomb interaction could be an orbital hybridization between excitonic levels of semiconductors (in organic framework, PbX_4 or PbX_3) and molecular orbitals of chiral molecules. While the explanation and experimental evidence for this mechanism are still elusive, this latent electronic interaction can facilitate chirality transfer to boost chiroptical activities.

Waldeck et al. first suggested that the chirality of the chiral shell (*R*- or *S*-PEA) could be imprinted onto the excitonic transition states of colloidal perovskite nanoplatelets (methylammonium lead bromide, $MAPbBr_3$).[52] As shown in **Figure 7**a (right panel), the CD spectra of chiral nanoplatelet dispersion exhibited an interesting behavior in the two regions of 300–350 and 400–450 nm. Neither PEA nor PEA-Br exhibited chiroptical response for wavelengths longer than 280 nm. Therefore, the two absorption responses of nanoplatelets in CD spectra were attributed to the chirality transfer from *R*- or *S*-PEA to $MAPbBr_3$. The bisignate peaks around 400 and 450 nm were located near the first excitonic transition band edge of $MAPbBr_3$ (Figure 7a, left panel), implying that the chiral PEA ligand imprinted its chirality onto the excitonic states of $MAPbBr_3$. The signal generated in the range 300–350 nm was ascribed to the charge transfer electronic states between PEA and $MAPbBr_3$. To prove the electronic interaction induced chirality transfer mechanism, temperature-dependent CD spectroscopy was conducted from 20 to 50 °C in the presence of excess chiral PEA ligands. As shown in Figure 7b, the CD intensity in the excitonic transition region of 400–450 nm remained almost unchanged, whereas a significant decrease was observed in the charge transfer region as the temperature increased. Additionally, with increasing temperature, the surface coverage of the chiral ligand gradually decreased and the charge transfer between chiral ligand and perovskite surface was hindered, which resulted in decreased CD intensity in the region 300–350 nm. However, irrespective of chiral ligand surface coverage, the persistent chiroptical feature appearance, which was imprinted onto the excitonic states (as identified by CD intensity at 400–450 nm), implies that the chirality transfer induced by Coulomb interaction could exist even in the absence of strong chiral molecules adsorbed on the surface.

To better understand the chirality transfer process through electronic interaction, a recent study on chiral QDs by Ben-Moshe et al. offers useful insight.[54] The detailed analysis of CD line shapes for CdSe and CdS QDs demonstrates that all the features in the complex CD spectra can be assigned to different excitonic transitions of QDs (Figure 7c,d). This suggests that coupling between the dipole transition of chiral molecules and QDs can split the excitonic states into two nondegenerate substates even in the absence of an external magnetic field. This justifies the mechanism by which the induced CD is derived from the electronic interaction between the highest occupied molecular orbital (HOMO) level and valence band (VB) hole level, as supported by the calculation results based on the density functional theory (DFT).[53] The electronic interaction was suggested as an actual hybridization between the hole state of QDs and molecular electronic state of chiral molecules.

The features of CD spectra of (*R*- and *S*-α-PEA)PbI_3 can also be interpreted as the interaction between the excitonic

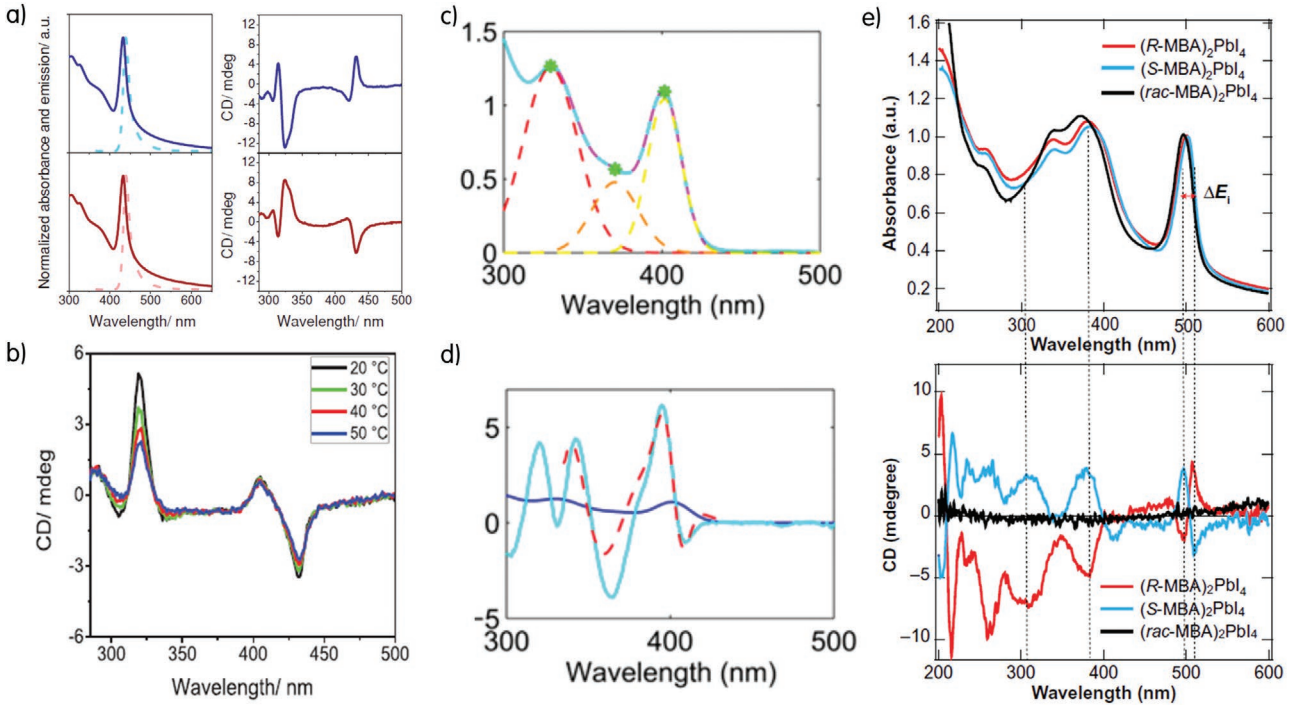

Figure 7. Chirality transfer in OIHPs induced by the electronic interaction between chiral molecules and achiral perovskites. a) Absorption (solid line) and emission (dashed line) spectra of *S*-PEA (blue) and *R*-PEA (red) based on perovskite nanoplatelets in toluene solutions (left panel). The CD spectra of chiral nanoplatelets in toluene solutions (right panel). b) Temperature-dependent CD spectra of chiral nanoplatelets in a solution with excess ligands. Reproduced with permission.[52] 2018, Wiley-VCH. Analysis of c) absorption spectra and d) CD spectra of CdS QDs. Reconstruction of the UV–vis absorption and CD spectra using the Gaussian function represented in dashed colored lines, where the green dots indicate their maxima. These peaks can be assigned to different excitonic transitions. Reproduced with permission.[53] Copyright 2019, American Chemical Society. e) Absorbance spectra (upper) and CD spectra (lower) of (*R*-, *S*-, rac-MBA)$_2$PbI$_4$. Reproduced with permission.[54] Copyright 2019, AAAS.

transition state of $(PbI_6)^{4-}$ octahedral and the transition dipole moment of the chiral α-PEA$^+$ cation.[45] Interestingly, both (*R*- and *S*-α-PEA)PbI$_3$ exhibited a monosignate Cotton effect (i.e., (*R*-α-PEA)PbI$_3$ for negative and (*S*-α-PEA)PbI$_3$ for positive) unlike the bisignate Cotton effect observed in common chiral composite systems. Based on the net rotational strength theory as described in Section 2.2 and Equation (2), the behavior of the monosignate Cotton effect in (*R*- and *S*-α-PEA)PbI$_3$ could be explained by the 3D arrangement of chiral molecules and the angle between each transition dipole moment (θ in Equation 2). Additionally, the CD spectra of thin films exhibited two strong peaks at 328 and 392 nm with intensities of 183 and 210 mdeg, respectively. This implies that two excitonic transition states were allowed in (*R*- and *S*-α-PEA)PbI$_3$.

Recently, Vardeny et al. reported similar phenomena where several peaks corresponding to multiple excitonic transition in low-dimensional perovskites were observed in the CD spectra.[54] As shown in Figure 7e, the exciton splitting energy (ΔE_i) of 51 meV was consistent with the difference between the two split exciton sublevels ($\Delta E_i \approx$ 20–50 meV) with opposite angular momentum. This confirmed that the resulting exciton splitting and chiroptical activity originated from the orbital hybridization, as discussed in Section 3.4. Thus, understanding the latent electronic interaction between transition dipole moments is necessary to further enhance the chiroptical properties of chiral perovskites.

4.4. Chiral Perovskite-Based Next-Generation Photonic Device

CPL is an indispensable light source in next-generation photonic devices such as quantum computation, drug screening, optical information process, and quantum optics. In the chiral photonics, LCP and RCP can be considered as two possible independent channels, where the rate of data transportation is twice that of unpolarized light. However, the conventional polarized light detecting and emitting devices make the configurations complicated with additional optical elements (i.e., waveplate, polarizer, filter), which is incompatible with highly integrated photonic circuits for ultra-fast data processing rate. Therefore, for realizing the practical application of chiral photonic devices, high-performance CPL detectors (CPL-PDs) and CPPL phenomena-based emitting device should be developed. In addition to CPL generating/sensing devices, the strong nonlinear response is also desirable for next-generation integrated photonic circuits.

4.5. CPL Detecting Device Based on Chiral OIHPs

Owing to their exceptional low trap density, strong light absorption ability, and broad wavelength tunability, several CPL-PDs based on chiral OHIPs as light absorbing layer was reported. First, 1D (*R*- and *S*-α-PEA)PbI$_3$ thin films were successfully employed in CPL-detecting devices owing to strong selective

absorption properties (CD intensity over ±150 mdeg) with a responsivity of 0.12 A W^{-1} under 395 nm irradiation.[45] This high responsivity value is almost two orders of magnitude larger than the conventional CPL-PDs based on other inorganic materials systems. Another key figure-of-merit performance parameter for CPL-PDs is distinguishability (g_{res}), which is the difference in the responsivities under RCP and LCP illumination. The calculated g_{res} value of CPL-PDs based on (*R*- and *S*-α-PEA)PbI_3 was 0.1, demonstrating the potential of chiral OIHPs for use in advanced optics and photonic devices.

Inspired by this development, CPL-PDs based on microplate chiral 2D OIHP with lateral configuration was also reported as shown in **Figure 8**a. The device showed significant high responsivity value of 0.45 A W^{-1} at a bias of 3 V and the calculated g_{res} value was 0.09 at 510 nm (Figure 8b), which is similar to that of CPL-PDs based on 1D chiral OIHPs.[43] Very recently, flexible CPL-PD with quasi-2D chiral OIHPs, $[(R)$-β-$MPA]_2MAPb_2I_7$ ((*R*)-β-MPA: *R*-(+)-β-methylphenethylamine; MA: methylammonium) exhibited excellent CPL detection performance with a g_{res} of 0.2 and responsivity of 1.1 A W^{-1}, respectively (Figure 8c,d).[55] Through the modulation of crystallization dynamics for the quasi-2D chiral OIHPs thin films, parallel oriented films with homogeneous energy alignment was obtained, maximizing the carrier collection efficiency.

Although the device performance of CPL-PDs (both responsivity and g_{res}) has been gradually enhanced, the key parameters of CPL-PDs are still far poor to meet the requirements for practical applications. Therefore, various strategies for better crystallinity and highly oriented thin films, ordered stacking of chiral molecules in inorganic framework of OIHPs, and interfacial engineering for carrier selective layers are highly demanded.

4.6. Chiral OIHPs as CPL Emitting Source

In addition to quantum data transportation and spin-based computation, CPL can be also applied as a direct light source of display applications. For instance, the direct emission of CPL has been recognized as an effective way to improve the performance of conventional light-emitting diodes (LEDs). In the conventional LEDs, to prevent reflection of ambient light from a metal electrode, a circular polarizer in front of the panel should be required. Therefore, only half of the light from the light emitting source reaches the human eye. To overcome this brightness-loss issue of conventional LEDs, light source which emits the light with the same handedness as in the circular polarizer in front of the panel is necessary.

Although the OIHPs have been definitely demonstrated as efficient light source for LEDs due to their high external quantum efficiencies (over 20%), the chiral OIHPs with a high anisotropic factor and photoluminescence quantum yields (PLQYs) at the same time have been rarely reported. To achieve CPL with high anisotropic factor in chiral OIHPs, large molecular fraction of the chiral organic spacer cations with respect to the achiral inorganic framework (e.g., $PbBr_4$) was required.[43] However, as the more chiral organic spacer cations were incorporated, the dimension of chiral OIHPs decreased, resulting in poor PLQYs at room temperature due to high non-radiative recombination rate.[42] Through the modulation of chiral OIHPs dimension, Long et al. reported a quasi-2D chiral perovskite with a PLQY of 90% and anisotropic factor of 3% in the absence of an external magnetic field. These high PLQYs and large anisotropic factor result from the efficient energy funneling process and effective chirality transfer, respectively.[42] Very recently, Kim et al. reported that colloidal chiral OIHPs

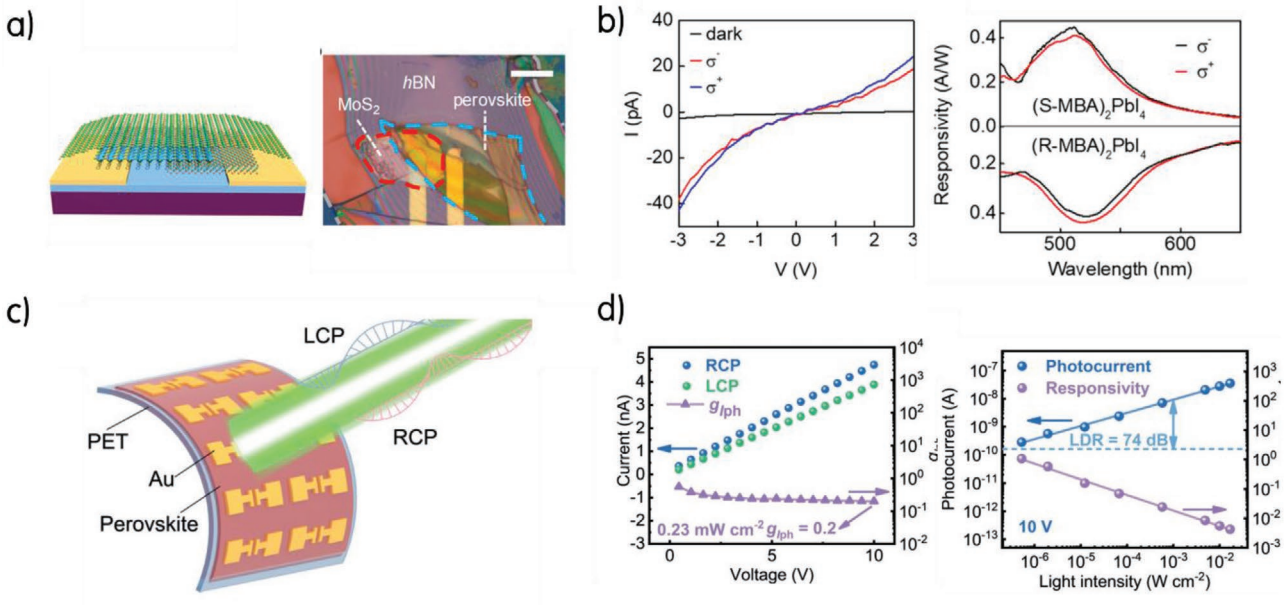

Figure 8. CPL-PD adopting the chiral OIHPs as light absorbing materials. a) Schematic (left panel) and optical image (right panel) of the two-probe lateral heterostructural device. b) Current–voltage curve of CPL-PD in the dark and under a 518 nm left-handed and right-handed CPL illumination (left panel) and spectral responsivity of CPL-PDs under different handedness of CPL illumination (right panel). Reproduced with permission.[43] Copyright 2019, American Chemical Society. c) Schematic illustration of flexible CPL-PD. d) Current–voltage curves and calculated g_{res} of flexible CPL-PD (left panel) and photocurrent and corresponding responsivity of CPL-PD. Reproduced with permission.[55] 2020, Wiley-VCH.

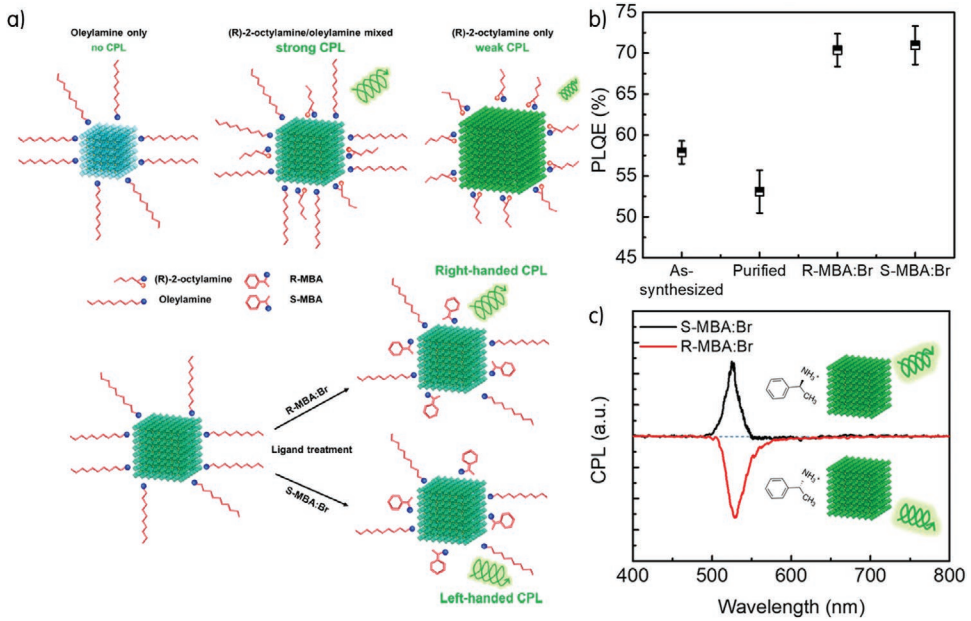

Figure 9. Chiral OIHPs as CPL emitting source. a) Schematic illustration of synthesis of formamidinium lead tribromide ($FAPbBr_3$) NCs with different ligand environment and postsynthetic ligand treatment. b) PLQY of as-synthesized $FAPbBr_3$ NCs, purified NCs, and after postsynthetic ligand treatment with chiral ligand. c) CPPL spectra of $FAPbBr_3$ NCs after post-synthetic ligand treatment with different handed chiral ligand. Reproduced with permission.[56] Copyright 2020, American Chemical Society.

NCs could exhibit CPL with anisotropic factor of 6.8% and PLQY of 60%, even at room temperature using chiral surface ligand exchange (**Figure 9**a,b).[56] In addition, the postsynthetic ligand treatment using *R*- or *S*-methylbenzylammonium bromide after purification process of NCs also induces a CPL with anisotropic factor of 1.18% (Figure 9c).

At the current stage, the CPL emitting efficiency of chiral OIHPs (both PLQY and anisotropic factor) is insufficient to replace the conventional LEDs. However, in a long-term perspective, the miniature, integrated devices without complicated configuration will play a pivotal role in implementing future photonic device and spin-based applications. Therefore, exploration of novel chiral moiety with strong chirality is needed, while obtaining better understanding of temperature dependent chiroptical behavior of chiral OIHPs.

4.7. Nonlinear Optical Response of Chiral OIHPs

Recently, OIHPs have been extensively studied as promising nonlinear optical (NLO) materials for diverse advanced photonic devices due to their versatile chemical compositions and large NLO coefficients. Even though the OIHPs with third- and high-order NLO effects are widely investigated and applied to optical devices, the materials with second-order NLO response is highly demanded for next-generation integrated photonic circuits. To achieve the second-order NLO response such as second harmonic generation (SHG), a strict structural noncentrosymmetry is essential. Therefore, chiral OIHPs with inherent noncentrosymmetry, which can create nonvanishing ETDM, have been recognized as a promising material exhibiting SHG phenomena. Yuan et al. reported that chiral OIHPs nanowire was crystallized in a noncentrosymmetric *P*1 space group, exhibiting strong SHG with high polarization ratios.[47a] Intercalation of dimethylsulfoxide (DMSO) molecules and chiral amine molecules into the perovskite lattice led to partial edge sharing and distorted layered structure (**Figure 10**a). As shown in Figure 10b, highly efficient SHG could be confirmed at different pumping wavelengths. In addition, at 850 nm pumping wavelength, the second-order NLO susceptibility was estimated to be 0.68 pm V^{-1}, which is comparable to prototypical material such as potassium dihydrogen phosphate. Synthesis of $(MPEA)_{1.5}PbBr_{3.5}(DMSO)_{0.5}$ (MPEA: methylphenethylamine) demonstrated the feasibility to realize the NLO effects in chiral OIHPs and expanded the potential applicability of chiral OIHPs to further important polarization-based devices such optical parametric generators and oscillators, and optical switches (Figure 10c).

4.8. Photoinduced Spin Signal Device with Chiral OIHPs

In addition to the well-established CPL detecting devices, CPL emitting phenomena, and NLO response, it was recently discovered that chiral OIHPs can be also utilized to spin injection and detection-based devices. As shown in **Figure 11**a, the chiral-induced spin selectivity (CISS) could occur when the chiral organic spacer of chiral OIHPs allows the one of the spin states (e.g., up-spin or down-spin state) to transport through the organic spacer while blocking the other spin state.[49,54] Using magnetic conductive-probe atomic force microscopy, Lu et al. demonstrated that oriented and layered chiral 2D OIHPs exhibited CISS phenomena.[54] Vertical electron transport through the layered chiral 2D OIHPs depends on the magnetization of the probe tip (up- and down-spin) and the configuration of chiral molecules (*R*- or *S*-MBA). As shown in Figure 11b, the

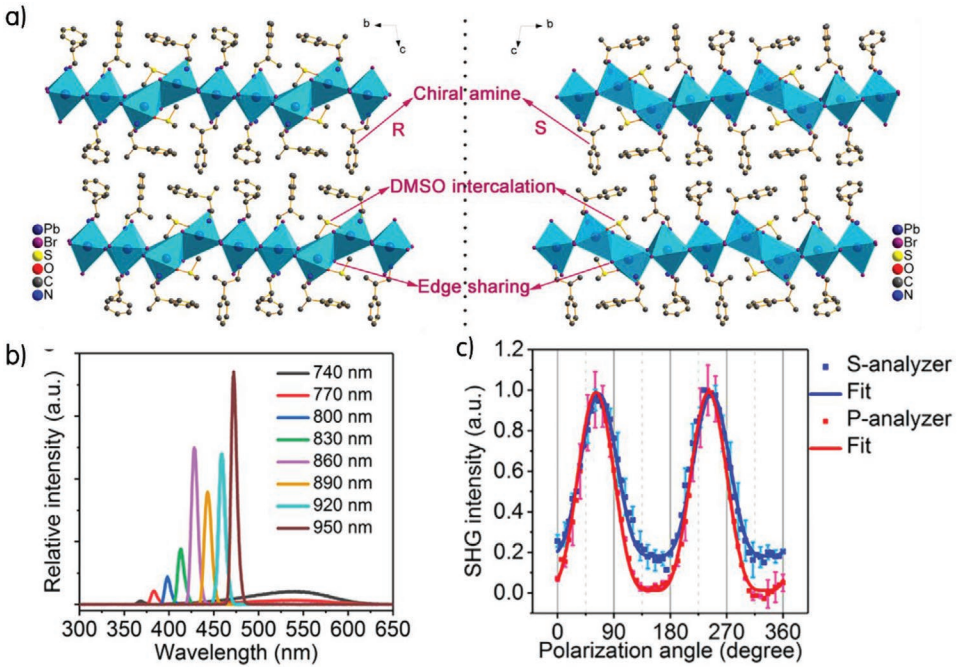

Figure 10. NLO response of chiral OIHPs. a) Crystallographic structure of the chiral OIHPs obtained from the single crystal XRD measurement, showing the partial edge sharing, distorted lattice, and DMSO intercalation. b) NLO spectra of $(MPEA)_{1.5}PbBr_{3.5}(DMSO)_{0.5}$ nanowire pumped at various wavelengths, normalized by the incident laser power. c) SHG intensity from the $(R\text{-}MPEA)_{1.5}PbBr_{3.5}(DMSO)_{0.5}$ nanowire as a function of the linear polarization angle. Reproduced with permission.[47a] Copyright 2018, American Chemical Society.

chiral OIHPs thin films revealed the highest anisotropic transport up to 86%, and were successfully applied to spin-valve devices having only one ferromagnet electrode. In the subsequent report in 2020, the synthesis of highly distorted tin-based 2D chiral OIHPs demonstrated an improved spin-polarization in the current-voltage characteristics as high as 94%.[57]

Furthermore, unlike achiral materials, the chiral OIHPs could generate the spin-polarized carriers in the absence of the magnetic field or a circularly polarized excitation, owing to inherent spin-polarized absorption and emission properties.[42] By combing the CISS phenomena and spin-polarized absorption properties of chiral OIHPs, Huang et al. recently reported novel proof-of-concept device with a configuration of NiFe/chiral OIHP/indium tin oxide heterostructure.[58] Upon illumination with 405 nm low-intensity laser, spin-polarized photocurrent generated in chiral OIHP layer gave rise to an increased magnetization of the NiFe film (Figure 11c). As shown in Figure 11d, the photoinduced Kerr signal exhibited linear dependence on the magnetic field and has opposite sign of slope for two enantiomers (positive to *R*-OIHPs and negative to *S*-OIHPs, respectively). This work demonstrated that the CISS effect can be potentially linked with the next-generation chiral photonic devices and Kerr signal is easily switched by the chirality of OIHPs.

5. Conclusion and Future Prospects

Since chiroptical properties of chiral perovskites were first examined in 2017, chiral perovskites have been extensively studied for chiral photonics and other optoelectronic applications within an extremely short duration. Given this trend, a gradual increase in studies exploring chiroptical properties is expected. Although numerous compositions of chiral perovskites have been reported and the magnitude of asymmetric properties being discovered has rapidly increased, an in-depth understanding of the origin of chirality transfer is still elusive. Therefore, this review focuses on providing useful information (e.g., fundamental basis of chirality and chirality transfer mechanism) to apprehend the origin of rare chiroptical phenomena. As chiroptical activities include several quantum physics phenomena, it is rather difficult to clearly define the origin of the chiroptical response. However, understanding the possible chirality transfer mechanisms can provide an effective approach to enhance the asymmetric response to CPL. Furthermore, this review also provides several bottlenecks of chiral OIHPs to be overcome and future direction to fully exploit the potential of this smart chiral material systems.

5.1. Controlled Crystallization Process for High-Quality Chiral OIHPs

As the most reported chirality of chiral OIHPs originates from the spatial arrangement of constituent atoms (e.g., induced by either surface distortion or inherent chiral crystal structure), the optimization of synthesis procedures is highly recommended to obtain high-quality chiral OIHP crystals. The anisotropic absorption factor for the reported chiral OIHPs remains low at approximately 10^{-2}–10^{-3}. Moreover, 10.1% of the luminescence dissymmetry ratio is obtained only at an ultralow temperature of 77 K, which completely disappears at room temperature due

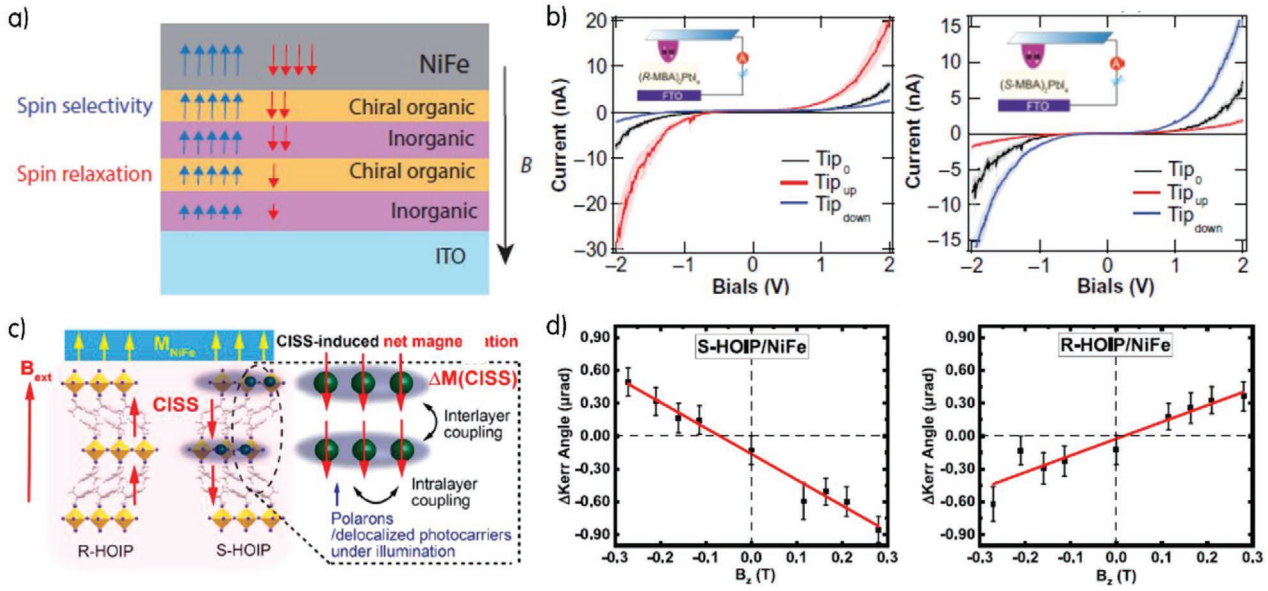

Figure 11. Photoinduced spin signal device with chiral OIHPs. a) Schematic illustration describing the spin selectivity phenomena in chiral OIHPs. b) Current–voltage curve of $(R\text{-MBA})_2PbI_4$ (left panel) and $(S\text{-MBA})_2PbI_4$ (right panel) measured by magnetic conductive-probe atomic force microscopy at room temperature. Reproduced with permission.[54] Copyright 2019, AAAS. c) Schematic illustration of the proposed photo-induced magnetization at the ferromagnet/chiral OIHP interface. d) Change of Kerr angle induced by photon absorption in *S*-configuration (left panel) and *R*-configuration (right panel) as a function of external magnetic field. Reproduced with permission.[58] Copyright 2020, American Chemical Society.

to phonon–electron interactions. Therefore, to exploit unique chiral OIHPs for practical device applications, high-quality thin films should be synthesized while preserving their chiral properties even in the thin film configuration as observed in the colloidal or bulk single crystal state. Therefore, extensive research is required to control crystallization kinetics via the Lewis adduct approach and additive engineering to obtain high-quality monolithic thin films with predicted morphology and shape. These synthetic strategies have been widely utilized for the fabrication of achiral OIHPs.[59] Additionally, an in-depth study of ligand chemistry is essential for rationally selecting suitable chiral capping ligands and synthesis conditions (e.g., solvent, concentration, and temperature). Introducing a chiral solvent during crystallization or low-dimensional OIHP growth[60] might be a promising strategy for further promoting the structure-induced chirality transfer.

5.2. Elucidating the Chiral Transfer Mechanism for Enhanced Chiroptical Phenomena

As mentioned above, most recent researches on chiral OIHPs mainly focus on the spatial rearrangement of atoms or inherent crystal structure of OIHPs. Compared with the straightforward mechanism (aforementioned in Sections 4.1 and 4.2), the effect of electronic interaction between the excitonic state of the achiral inorganic framework (i.e., PbX_4 or PbX_3) and molecular orbital of chiral molecules has been underestimated and is still elusive. However, synergetic effect of electronic interaction and structural chirality can further amplify the existing chiroptical properties.

At first, the manner in which electronic interaction contributes to the chiroptical behavior of chiral perovskites should be understood. As each peak of CD spectra can be assigned to different excitonic transitions of OIHPs, deconvolution of CD spectra will help unveil the underlying physical phenomena for excitonic transition in chiral perovskites. Additionally, as low-dimensional perovskites exhibit multiple excitonic transition behavior,[42,61] (e.g., 1D, 2D, and quasi-2D OIHPs) they would become an ideal platform to scrutinize the transitional behavior of chiral perovskites. For appropriate chiral molecules or cations, the HOMO level of such a molecule/cation should be considered in terms of its efficient hybridization capability with the VB level of OIHPs. Recent work by Gao et al. reported that a large π bond (Π_6^6) with delocalized electron of spacer could effectively change the electronic configuration of quasi-2D OIHPs, demonstrating the potential coupling effect of π-electron of organic spacer and p orbital of I^- from the inorganic framework.[62] Therefore, through the delicate control of the electronic interaction between the chiral organic molecules and achiral inorganic framework, it is highly expected that chiral OIHPs could further deliver the enhanced chiroptical activity and large anisotropic optical behavior. In this perspective, chiral molecules with high ETDM or MTDM should also be considered as candidates for the synthesis of new chiral OIHPs because chiroptical activity is influenced by ETDM and MTDM. Furthermore, DFT calculations describing the electronic structures of chiral molecules could provide a new synthetic strategy for designing various chiral OIHPs with large chiroptical activity.

5.3. 3D Chiral Perovskite for Broadband Chiroptical Phenomena

Because of the large size of chiral organic molecules, most current studies on chiral OIHPs have been limited to OIHPs with

low <*n*> values (e.g., $RPbX_3$ or R_2PbX_4; X = halide ion, R = large sized aromatic amine). However, most reported OIHPs with low <*n*> values (<*n*> = 1 or 2) likely suffer from significant non-radiative recombination and poor PLQY, thus hampering them from being utilized in optoelectronic applications. Additionally, to develop practical optoelectronic devices, the wavelength tunability of chiroptical phenomena is required.[46] Compared with their low <*n*> counterparts, quasi-2D and 3D chiral perovskites with a narrow bandgap are capable of showing chiroptical activities in the longer wavelength region. Fortunately, a recent theoretical calculation successfully predicted that 3D chiral perovskites would be stable with chiral cations such as $CHFClNH_3^+$ or $CHDFNH_3^+$.[63] Additional, Yuan et al. discussed CPL-PDs that possess exceptional semiconducting properties based on quasi-2D chiral perovskites.[55] Therefore, phase control of chiral quasi-2D perovskite or novel design of chiral 3D perovskites with the smallest chiral monovalent cation (e.g., $CHFClNH_3^+$ or $CHDFNH_3^+$) exhibit excellent potential in chiral photonics. In addition, the colloidal OIHP NCs with chiral ligand become the one of possible candidates for widening the wavelength region of chiroptical phenomena due to their controllable size-dependent quantum confinement effect, high PLQY, and extensive compositional tunability.[56]

Acknowledgements

This work was supported by a National Research Foundation (NRF) of Korea grant (No. 2012R1A3A2026417) funded by the Ministry of Science and ICT.

Conflict of Interest

The authors declare no conflict of interest.

Keywords

chiral perovskites, chirality transfer mechanism, circular dichroism, circularly polarized luminescence

Received: August 24, 2020
Revised: October 9, 2020
Published online:

[1] a) N. Gisin, R. Thew, *Nat. Photonics* **2007**, *1*, 165; b) R. F. Service, *Science* **2001**, *292*, 2412; c) S. K. Liao, W. Q. Cai, J. Handsteiner, B. Liu, J. Yin, L. Zhang, D. Rauch, M. Fink, J. G. Ren, W. Y. Liu, Y. Li, Q. Shen, Y. Cao, F. Z. Li, J. F. Wang, Y. M. Huang, L. Deng, T. Xi, L. Ma, T. Hu, L. Li, N. L. Liu, F. Koidl, P. Y. Wang, Y. A. Chen, X. B. Wang, M. Steindorfer, G. Kirchner, C. Y. Lu, R. Shu, R. Ursin, T. Scheidl, C. Z. Peng, J. Y. Wang, A. Zeilinger, J. W. Pan, *Phys. Rev. Lett.* **2018**, *120*, 030501; d) P. C. Humphreys, N. Kalb, J. P. J. Morits, R. N. Schouten, R. F. L. Vermeulen, D. J. Twitchen, M. Markham, R. Hanson, *Nature* **2018**, *558*, 268.

[2] a) J. Y. Wang, C. Zhang, H. L. Liu, R. McLaughlin, Y. X. Zhai, S. R. Vardeny, X. J. Liu, S. McGill, D. Semenov, H. W. Guo, R. Tsuchikawa, V. V. Deshpande, D. L. Sun, Z. V. Vardeny, *Nat. Commun.* **2019**, *10*, 129; b) J. M. Abendroth, D. M. Stemer, B. P. Bloom, P. Roy, R. Naaman, D. H. Waldeck, P. S. Weiss, P. C. Mondal, *ACS Nano* **2019**, *13*, 4928; c) R. Naaman, Y. Paltiel, D. H. Waldeck, *Nat. Rev. Chem.* **2019**, *3*, 250.

[3] a) H. K. Bisoyi, Q. Li, *Acc. Chem. Res.* **2014**, *47*, 3184; b) M. Schadt, *Annu. Rev. Mater. Sci.* **1997**, *27*, 305.

[4] a) D. J. Kissick, D. Wanapun, G. J. Simpson, *Annu. Rev. Anal. Chem.* **2011**, *4*, 419; b) H. Lee, M. J. Huttunen, K. J. Hsu, M. Partanen, G. Y. Zhuo, M. Kauranen, S. W. Chu, *Biomed. Opt. Express* **2013**, *4*, 909.

[5] M. I. Dyakonov, *Phys. E* **2006**, *35*, 246.

[6] a) N. Berova, L. Di Bari, G. Pescitelli, *Chem. Soc. Rev.* **2007**, *36*, 914; b) A. O. Govorov, Z. Y. Fan, P. Hernandez, J. M. Slocik, R. R. Naik, *Nano Lett.* **2010**, *10*, 1374.

[7] J. K. Kowalska, J. T. Henthorn, C. Van Stappen, C. Trncik, O. Einsle, D. Keavney, S. DeBeer, *Angew. Chem., Int. Ed.* **2019**, *58*, 9373.

[8] a) J. P. Riehl, F. S. Richardson, *Chem. Rev.* **1986**, *86*, 1; b) C. D. Tran, G. S. Beddard, *J. Am. Chem. Soc.* **1982**, *104*, 6741.

[9] C. D. Tran, G. S. Beddard, *Biochim. Biophys. Acta* **1981**, *678*, 497.

[10] a) L. Ripa, A. Hallberg, J. Sandstrom, *J. Am. Chem. Soc.* **1997**, *119*, 5701; b) L. Di Bari, G. Pescitelli, P. Salvadori, *J. Am. Chem. Soc.* **1999**, *121*, 7998.

[11] a) F. Hao, C. C. Stoumpos, R. P. H. Chang, M. G. Kanatzidis, *J. Am. Chem. Soc.* **2014**, *136*, 8094; b) S. A. Kulkarni, T. Baikie, P. P. Boix, N. Yantara, N. Mathews, S. Mhaisalkar, *J. Mater. Chem. A* **2014**, *2*, 9221; c) R. Prasanna, A. Gold-Parker, T. Leijtens, B. Conings, A. Babayigit, H. G. Boyen, M. F. Toney, M. D. McGehee, *J. Am. Chem. Soc.* **2017**, *139*, 11117.

[12] a) S. Ma, S. H. Kim, B. jeong, H. C. Kwon, S. C. Yun, G. Fang, H. Yang, C. Park, D. Lee, J. Moon, *Small* **2019**, *15*, 1900219; b) B. Jeong, H. Han, Y. J. Choi, S. H. Cho, E. H. Kim, S. W. Lee, J. S. Kim, C. Park, D. Kim, C. Park, *Adv. Funct. Mater.* **2018**, *28*, 1706401.

[13] K. Galkowski, A. Mitioglu, A. Miyata, P. Plochocka, O. Portugall, G. E. Eperon, J. T. W. Wang, T. Stergiopoulos, S. D. Stranks, H. J. Snaith, R. J. Nicholas, *Energy Environ. Sci.* **2016**, *9*, 962.

[14] a) Q. F. Dong, Y. J. Fang, Y. C. Shao, P. Mulligan, J. Qiu, L. Cao, J. S. Huang, *Science* **2015**, *347*, 967; b) S. D. Stranks, G. E. Eperon, G. Grancini, C. Menelaou, M. J. P. Alcocer, T. Leijtens, L. M. Herz, A. Petrozza, H. J. Snaith, *Science* **2013**, *342*, 341; c) G. C. Xing, N. Mathews, S. Y. Sun, S. S. Lim, Y. M. Lam, M. Gratzel, S. Mhaisalkar, T. C. Sum, *Science* **2013**, *342*, 344.

[15] C. Zhang, D. Sun, C. X. Sheng, Y. X. Zhai, K. Mielczarek, A. Zakhidov, Z. V. Vardeny, *Nat. Phys.* **2015**, *11*, 427.

[16] a) M. Isarov, L. Z. Tan, M. I. Bodnarchuk, M. V. Kovalenko, A. M. Rappe, E. Lifshitz, *Nano. Lett.* **2017**, *17*, 5020; b) E. Mosconi, T. Etienne, F. De Angelis, *J. Phys. Chem. Lett.* **2017**, *8*, 2247; c) D. Niesner, M. Wilhelm, I. Levchuk, A. Osvet, S. Shrestha, M. Batentschuk, C. Brabec, T. Fauster, *Phys. Rev. Lett.* **2016**, *117*, 126401; d) P. Odenthal, W. Talmadge, N. Gundlach, R. Z. Wang, C. Zhang, D. L. Sun, Z. G. Yu, Z. V. Vardeny, Y. S. Li, *Nat. Phys.* **2017**, *13*, 894.

[17] F. Pulizzi, *Nat. Mater.* **2012**, *11*, 367.

[18] D. G. Billing, A. Lemmerer, *Acta Crystallogr.* **2003**, E*59*, 381.

[19] D. G. Billing, A. Lemmerer, *CrystEngComm* **2006**, *8*, 686.

[20] J. Ahn, E. Lee, J. Tan, W. Yang, B. Kim, J. Moon, *Mater. Horiz.* **2017**, *4*, 851.

[21] a) Y. Z. Dong, Y. P. Zhang, X. Y. Li, Y. Q. Feng, H. Zhang, J. L. Xu, *Small* **2019**, *15*, 1902237; b) G. K. Long, R. Sabatini, M. I. Saidaminov, G. Lakhwani, A. Rasmita, X. G. Liu, E. H. Sargent, W. B. Gao, *Nat. Rev. Mater.* **2020**, *5*, 423.

[22] N. Kobayashi, A. Muranaka, J. Mark, *Circular Dichroism and Magnetic Circular Dichroism Spectroscopy for Organic Chemist*, Royal Society of Chemistry, Cambridge **2012**.

[23] J. A. Schellman, P. Oriel, *J. Chem. Phys.* **1962**, *37*, 2114.

[24] J. Sändstrom, in *Circular Dichroism: Principles and Applications*, 2nd ed., (Eds: N. Berova, K. Nakanishi, R. W. Woody), Wiley-VCH, New York **2000**, Ch. 16.
[25] M. J. Yuan, L. N. Quan, R. Comin, G. Walters, R. Sabatini, O. Voznyy, S. Hoogland, Y. B. Zhao, E. M. Beauregard, P. Kanjanaboos, Z. H. Lu, D. H. Kim, E. H. Sargent, *Nat. Nanotechnol.* **2016**, *11*, 872.
[26] a) C. Gautier, T. Burgi, *J. Am. Chem. Soc.* **2006**, *128*, 11079; b) J. M. Ha, A. Solovyov, A. Katz, *Langmuir* **2009**, *25*, 153; c) T. H. Li, H. G. Park, H. S. Lee, S. H. Choi, *Nanotechnology* **2004**, *15*, S660; d) C. E. Roman-Velazquez, C. Noguez, I. L. Garzon, *J. Phys. Chem. B* **2003**, *107*, 12035; e) G. Shemer, O. Krichevski, G. Markovich, T. Molotsky, I. Lubitz, A. B. Kotlyar, *J. Am. Chem. Soc.* **2006**, *128*, 11006; f) Z. Y. Tang, Y. Wang, S. Shanbhag, M. Giersig, N. A. Kotov, *J. Am. Chem. Soc.* **2006**, *128*, 6730.
[27] T. G. Schaaff, R. L. Whetten, *J. Phys. Chem. B* **2000**, *104*, 2630.
[28] M. R. Goldsmith, C. B. George, G. Zuber, R. Naaman, D. H. Waldeck, P. Wipf, D. N. Beratan, *Phys. Chem. Chem. Phys.* **2006**, *8*, 63.
[29] S. D. Elliott, M. P. Moloney, Y. K. Gun'ko, *Nano Lett.* **2008**, *8*, 2452.
[30] T. Nakashima, Y. Kobayashi, T. Kawai, *J. Am. Chem. Soc.* **2009**, *131*, 10342.
[31] a) A. Ben-Moshe, A. O. Govorov, G. Markovich, *Angew. Chem., Int. Ed.* **2013**, *52*, 1275; b) H. Peng, N. Kioussis, G. J. Snyder, *Phys. Rev. B* **2014**, *89*, 195206; c) O. Vogl, *J. Polym. Sci., Part A: Polym. Chem.* **2011**, *49*, 1299; d) P. P. Wang, S. J. Yu, A. O. Govorov, M. Ouyang, *Nat. Commun.* **2017**, *8*, 14312; e) K. C. Nomura, *Phys. Rev. Lett.* **1960**, *5*, 500.
[32] L. Sohncke, *Entwickelung einer Theorie der Krystallstruktur*, B.G. Teubner, Leipzig **1879**.
[33] a) A. Ben-Moshe, S. G. Wolf, M. Bar Sadan, L. Houben, Z. Y. Fan, A. O. Govorov, G. Markovich, *Nat. Commun.* **2014**, *5*, 4302. b) I. Dolamic, S. Knoppe, A. Dass, T. Burgi, *Nat. Commun.* **2012**, *3*, 798; c) O. Lopez-Acevedo, H. Tsunoyama, T. Tsukuda, H. Hakkinen, C. M. Aikens, *J. Am. Chem. Soc.* **2010**, *132*, 8210; d) H. F. Qian, W. T. Eckenhoff, Y. Zhu, T. Pintauer, R. C. Jin, *J. Am. Chem. Soc.* **2010**, *132*, 8280.
[34] H. E. Lee, H. Y. Ahn, J. Mun, Y. Y. Lee, M. Kim, N. H. Cho, K. Chang, W. S. Kim, J. Rho, K. T. Nam, *Nature* **2018**, *556*, 360.
[35] T. C. He, Y. Gao, Y. Gao, X. D. Lin, R. Chen, W. B. Hu, X. Zhao, Y. Wang, H. V. Demir, Q. L. Fan, A. C. Grimsdale, H. D. Sun, *Macromol. Chem. Phys.* **2016**, *217*, 24.
[36] Q. Zhang, T. Atay, J. R. Tischler, M. S. Bradley, V. Bulovic, A. V. Nurmikko, *Nat. Nanotechnol.* **2007**, *2*, 555.
[37] U. Tohgha, K. K. Deol, A. G. Porter, S. G. Bartko, J. K. Choi, B. M. Leonard, K. Varga, J. Kubelka, G. Muller, M. Balaz, *ACS Nano* **2013**, *7*, 11094.
[38] T. C. He, J. Z. Li, X. R. Li, C. Ren, Y. Luo, F. H. Zhao, R. Chen, X. D. Lin, J. M. Zhang, *Appl. Phys. Lett.* **2017**, *111*, 151102.
[39] W. J. Chen, S. Zhang, M. H. Zhou, T. H. Zhao, X. J. Qin, X. F. Liu, M. H. Liu, P. F. Duan, *J. Phys. Chem. Lett.* **2019**, *10*, 3290.
[40] a) F. Hidalgo, C. Noguez, *ACS Nano* **2013**, *7*, 513; b) A. Sanchez-Castillo, C. Noguez, I. L. Garzon, *J. Am. Chem. Soc.* **2010**, *132*, 1504.
[41] a) U. Tohgha, K. Varga, M. Balaz, *Chem. Commun.* **2013**, *49*, 1844; b) R. Zhou, K. Y. Wei, J. S. Zhao, Y. B. Jiang, *Chem. Commun.* **2011**, *47*, 6362.
[42] G. K. Long, C. Y. Jiang, R. Sabatini, Z. Y. Yang, M. Y. Wei, L. N. Quan, Q. M. Liang, A. Rasmita, M. Askerka, G. Walters, X. W. Gong, J. Xing, X. L. Wen, R. Quintero-Bermudez, H. F. Yuan, G. C. Xing, X. R. Wang, D. T. Song, O. Voznyy, M. T. Zhang, S. Hoogland, W. B. Gao, Q. H. Xiong, E. H. Sargent, *Nat. Photonics* **2018**, *12*, 528.
[43] J. Q. Ma, C. Fang, C. Chen, L. Jin, J. Q. Wang, S. Wang, J. Tang, D. H. Li, *ACS Nano* **2019**, *13*, 3659.
[44] L. M. Ni, U. Huynh, A. Cheminal, T. H. Thomas, R. Shivanna, T. F. Hinrichsen, S. Ahmad, A. Sadhanala, A. Rao, *ACS Nano* **2017**, *11*, 10834.
[45] C. Chen, L. Gao, W. R. Gao, C. Y. Ge, X. Du, Z. Li, Y. Yang, G. D. Niu, J. Tang, *Nat. Commun.* **2019**, *10*, 1927.
[46] J. Ahn, S. Ma, J. Y. Kim, J. Kyhm, W. Yang, J. A. Lim, N. A. Kotov, J. Moon, *J. Am. Chem. Soc.* **2020**, *142*, 4206.
[47] a) C. Q. Yuan, X. Y. Li, S. Semin, Y. Q. Feng, T. Rasing, J. L. Xu, *Nano Lett.* **2018**, *18*, 5411. b) B. Sun, X.-F. Liu, X.-Y. Li, Y. Zhang, X. Shao, D. Yang, H.-L. Zhang, *Chem. Mater.* **2020**, *32*, 8914; c) P. J. Huang, K. Taniguchi, H. Miyasaka, *J. Am. Chem. Soc.* **2019**, *141*, 14520;
[48] Y. Ai, X. G. Chen, P. P. Shi, Y. Y. Tang, P. F. Li, W. Q. Liao, R. G. Xiong, *J. Am. Chem. Soc.* **2019**, *141*, 4474.
[49] Y. Hui, F. Florio, Z. Z. Chen, W. A. Phelan, M. A. Siegler, Z. Zhou, Y. W. Guo, R. Hawks, J. Jiang, J. Feng, L. F. Zhang, B. W. Wang, Y. P. Wang, D. Gall, E. F. Palermo, Z. H. Lu, X. Sun, T. M. Lu, H. Zhou, Y. Ren, E. E. Wertz, R. A. S. K. R. Sundararaman, J. Shi, *Sci. Adv.* **2020**, *6*, eaay4213.
[50] Y. Peng, Y. P. Yao, L. N. Li, Z. Y. Wu, S. S. Wang, J. H. Luo, *J. Mater. Chem. C* **2018**, *6*, 6033.
[51] T. H. Moon, S. J. Oh, K. M. Ok, *ACS Omega* **2018**, *3*, 17895.
[52] Z. N. Georgieva, B. P. Bloom, S. Ghosh, D. H. Waldeck, *Adv. Mater.* **2018**, *30*, 1800097.
[53] A. Ben-Moshe, A. Teitelboim, D. Oron, G. Markovich, *Nano Lett.* **2016**, *16*, 7467.
[54] H. P. Lu, J. Y. Wang, C. X. Xiao, X. Pan, X. H. Chen, R. Brunecky, J. J. Berry, K. Zhu, M. C. Beard, Z. V. Vardeny, *Sci. Adv.* **2019**, *5*, eaay0571.
[55] L. Wang, Y. X. Xue, M. H. Cui, Y. M. Huang, H. Y. Xu, C. C. Qin, J. Yang, H. T. Dai, M. J. Yuan, *Angew. Chem., Int. Ed.* **2020**, *132*, 6504.
[56] Y. H. Kim, Y. X. Zhai, E. A. Gaulding, S. N. Habisreutinger, T. Moot, B. A. Rosales, H. P. Lu, A. Hazarika, R. Brunecky, L. M. Wheeler, J. J. Berry, M. C. Beard, J. M. Luther, *ACS Nano* **2020**, *14*, 8816.
[57] H. P. Lu, C. X. Xiao, R. Y. Song, T. Y. Li, A. E. Maughan, A. Levin, R. Brunecky, J. J. Berry, D. B. Mitzi, V. Blum, M. C. Beard, *J. Am. Chem. Soc.* **2020**, *142*, 13030.
[58] Z. J. Huang, B. P. Bloom, X. J. Ni, Z. N. Georgieva, M. Marciesky, E. Vetter, F. Liu, D. H. Waldeck, D. L. Sun, *ACS Nano* **2020**, *14*, 10370.
[59] a) E. H. Jung, N. J. Jeon, E. Y. Park, C. S. Moon, T. J. Shin, T. Y. Yang, J. H. Noh, J. Seo, *Nature* **2019**, *567*, 511; b) G. Jang, H. C. Kwon, S. Ma, S. C. Yun, H. Yang, J. Moon, *Adv. Energy Mater.* **2019**, *9*, 1901719; c) N. Ahn, D. Y. Son, I. H. Jang, S. M. Kang, M. Choi, N. G. Park, *J. Am. Chem. Soc.* **2015**, *137*, 8696; d) J. W. Lee, H. S. Kim, N. G. Park, *Acc. Chem. Res.* **2016**, *49*, 311.
[60] a) D. Lee, Y. J. Jin, H. Kim, N. Suzuki, M. Fujiki, T. Sakaguchi, S. K. Kim, W. E. Lee, G. Kwak, *Macromolecules* **2012**, *45*, 5379; b) B. Zhao, H. L. Yu, K. Pan, Z. A. Tan, J. P. Deng, *ACS Nano* **2020**, *14*, 3208.
[61] K. Tanaka, T. Takahashi, T. Kondo, K. Umeda, K. Ema, T. Umebayashi, K. Asai, K. Uchida, N. Miura, *Jpn. J. Appl. Phys.* **2005**, *44*, 5923.
[62] C. F. Gao, R. P. Li, Y. R. Li, R. Wang, M. Wang, Z. X. Gan, L. G. Ba, Y. C. Liu, K. Zhao, S. F. Liu, Y. C. Cheng, W. Huang, *J. Phys. Chem. Lett.* **2019**, *10*, 5687.
[63] G. K. Long, Y. C. Zhou, M. T. Zhang, R. Sabatini, A. Rasmita, L. Huang, G. Lakhwani, W. B. Gao, *Adv. Mater.* **2019**, *31*, 1807628.

Sunihl Ma is a Ph.D. candidate in the Department of Materials Science and Engineering at Yonsei University, Seoul, Korea, under the supervision of Dr. J. Moon. He received his B.S. in materials science and engineering from the Department of Materials Science and Engineering, Yonsei University, Korea, in 2016. His research includes the fabrication and application of halide perovskite materials for chiral photonics and optoelectronic devices.

Jooho Moon is a professor in the Department of Materials Science and Engineering at Yonsei University, Seoul, Korea. He holds an M.S. and Ph.D. in materials science and engineering from the University of Florida. He did his postdoctoral research in the Materials Processing Center at MIT. His research interests include printed electronics and displays, solid-oxide fuel cells, perovskite solar cells, and water splitting. He has coauthored more than 250 publications and has been serving as an associate editor of ACS Applied Materials & Interfaces since 2015.